JGR Planets

RESEARCH ARTICLE
10.1029/2018JE005799

Key Points:
- A pole to equator variation in insolation can drive *Hadley-like* convective cells in the ice shell, with polar downwelling and equatorial upwelling
- Velocity and surface deformation patterns can be diagnostic, with poleward compressive and equatorward extensional trends
- Latitudinal variation in surface temperature is likely an important effect for convection within the outer satellites

Supporting Information:
- Supporting Information S1
- Figure S1
- Figure S2
- Figure S3
- Figure S4
- Figure S5
- Table S1

Correspondence to:
M. B. Weller,
mbweller@brown.edu

Citation:
Weller, M. B., Fuchs, L., Becker, T. W., & Soderlund, K. M. (2019). Convection in thin shells of icy satellites: Effects of latitudinal surface temperature variations. *Journal of Geophysical Research: Planets*, *124*, 2029–2053. https://doi.org/10.1029/2018JE005799

Received 17 AUG 2018
Accepted 9 MAR 2019
Accepted article online 9 APR 2019
Published online 5 AUG 2019

Convection in Thin Shells of Icy Satellites: Effects of Latitudinal Surface Temperature Variations

Matthew B. Weller[1,2], Lukas Fuchs[1,3], Thorsten W. Becker[1,4], and Krista M. Soderlund[1]

[1]Institute for Geophysics, Jackson School of Geosciences, The University of Texas at Austin, Austin, TX, USA, [2]Now at Department of Earth, Environmental and Planetary Sciences, Brown University, Providence, RI, USA, [3]Now at Johann-Wolfgang Goethe Universität, Frankfurt, Germany, [4]Department of Geological Sciences, Jackson School of Geosciences, The University of Texas at Austin, Austin, TX, USA

Abstract We use three-dimensional numerical experiments of thin shell convection to explore what effects an expected latitudinal variation in solar insolation may have on a convection. We find that a global flow pattern of upwelling equatorial regions and downwelling polar regions, linked to higher and lower surface temperatures (T_s), respectively, is preferred. Due to the gradient in T_s, boundary layer thicknesses vary from equatorial lows to polar highs, and polar oriented flow fields are established. A *Hadley cell*-type configuration with two hemispheric-scale convective cells emerges with heat flow enhanced along the equator and suppressed poleward. The poleward transport pattern appears robust under a range of basal and mixed heating, isoviscous and temperature-dependent viscosity, vigor of convection, and different degrees of T_s variations. Our findings suggest that a latitudinal variation in T_s is an important effect for convection within the thin ice shells of the outer satellites, becoming increasingly important as solar luminosity increases. Variable T_s models predict lower heat flow and a more compressional regime near downwellings at higher latitudes, and higher heat flow and a more extensional regime near the equator. Within the ice shell, Hadley style flow could lead to large-scale anisotropic ice properties that might be detectable with future seismic or electro-magnetic observations.

Plain Language Summary Due to the curvature of planets, energy from the Sun varies from the equator to the poles. On airless bodies, such as the icy satellites, this difference in the Sun's energy leads to a variation in surface temperatures from an equatorial maximum to a polar minimum. This difference in surface temperatures for the icy satellites is a significant fraction of the temperature at the base of the ice shell or a significant fraction of the temperature differential that drives convection. We use numerical models of mantle convection in a three-dimensional sphere to show that a poleward transport of material from equatorial regions emerges. Models with latitudinally variable surface temperatures predict lower heat flow, thicker conductive regions, and a more compressional stress state near downwellings at high latitudes, and higher heat flow, thinner conductive regions, and a more extensional stress state near the equator. A latitudinal variation in surface temperatures is likely an important effect for convection and the expression of surface deformation of the icy outer satellites and becomes increasingly important as the Sun ages.

1. Introduction

The surfaces of the icy satellites within our solar system indicate a wide range of geologic activity, from relatively undeformed Callisto (e.g., Bender et al., 1997; Greeley et al., 2000; Moore et al., 2004) and Dione (Collins et al., 2010; Moore et al., 1985; Moore & Schenk, 2007; Wagner et al., 2006) to highly deformed Ganymede (e.g., McKinnon & Parmentier, 1986; Pappalardo et al., 2004), Miranda (e.g., Cameron et al., 2018; Smith et al., 1986; Zahnle et al., 2003), Enceladus (e.g., Barr & Preuss, 2010; Collins et al., 2010; Kirchoff & Schenk, 2009; Porco et al., 2006), and Europa (e.g., Greeley et al., 2004; Helfenstein & Parmentier, 1985; Kattenhorn & Prockter, 2014), the latter two currently active as evidenced from observed plumes(e.g., Jia et al., 2018; Spencer et al., 2009; Spitale & Porco, 2007). Explanations for the variations in activity range from external impact events to internal processes such as ice shell solidification and convection (e.g., Barr & Hammond, 2015; Grott et al., 2007; Hammond & Barr, 2014a, 2014b; McKinnon, 2006; Moore, 2006; Pappalardo et al., 1998; Sparks et al., 2017). Solid state convection is a particularly attractive solution as the outer satellites' ice shells likely have significant energy input from tidal heating, in addition to heating from the underlying silicate mantle.

Unraveling how heat is transferred in the outer ice shells is of key importance for understanding the thermal and dynamic evolution of icy bodies. The efficiency of heat transport, its spatial distribution, and the mode the transport takes across the outer shell controls the satellites' evolution, both in the interior as well as the styles of resurfacing and stress distribution within and on the surface of the ice shell. The long-term evolution in turn controls the existence as well as the longevity of any potential subsurface ocean and, consequently, is a significant control for the possibility for life on these worlds. As such, in order to understand the thermal and geodynamic evolution of icy satellites, and how these may or may not lead to clement conditions for life, we need to understand how ice convection behaves in response to physical processes and driving forces on the icy satellites.

Here we address the effect of latitudinally variable surface temperature (due to differences in solar heating; e.g., Nadeau & McGehee, 2017; Ojakangas & Stevenson, 1989) for isoviscous and temperature-dependent viscosity convection for pure basal and mixed heating systems with high internal heating rates (as proxy for tidal heating) on the convective vigor and planform within a thin ice shell of fixed thickness. The majority of studies of the icy satellites focus on Cartesian geometries (e.g., Barr, 2008; Barr & Hammond, 2015; Hammond & Barr, 2014a, 2014b; Han & Showman, 2010; O'Neill & Nimmo, 2010; Showman & Han, 2004, 2005) with relatively few exploring convection in thin shell geometries or in full spherical 3-D (e.g., Guerrero et al., 2018; Han et al., 2012; Roberts & Nimmo, 2008; Showman et al., 2013; Yao et al., 2014). The intent of this work is not to model convection in a specific icy satellite but instead to explore the effect of latitudinally variable surface temperatures in cases of thin shell convection that may be applied broadly to any icy satellite (and potentially Mercury and extrasolar planets, cf. van Summeren et al., 2011; Tosi et al., 2015). Our models are deliberately simple, so as to be able to isolate the effects of variable surface temperature on dynamics in full spherical 3-D systems before incorporating other complicating processes, such as tidal dissipation, in a subsequent study.

In order to evaluate the effects of latitudinal variation in surface temperature, we first focus on a simple system of basally heated, isoviscous convection. Subsequently, we add complexity by including varying degrees of temperature-dependent viscosity. Following this, we test the robustness and sensitivity of the system to a range of parameters. First, we consider the effects of a mixed heating system (combination of basal and internal heating to mimic tidal heating effects). Second, we test the sensitivity of our results by evaluating differing vigors of convection, and third we test the effects of the amplitude of surface temperature variations. We show that a latitudinal variation in solar insolation has a robust effect on all convective systems tested. It affects the planform of convection, velocity and strain distributions, and heat flux patterns, which have important and testable implications for the icy satellites.

2. Numerical Models and Methods

To model global convection in 3-D, spherical geometry, we use dimensionless forms of the governing equations for conservation of mass, momentum, and energy, assuming infinite Prandtl number and Boussinesq approximations:

$$u_{i,j} = 0 \tag{1}$$

$$-P_{,i} + \left(\eta\left(u_{i,j} + u_{j,i}\right)\right)_{,j} + RaT\delta_{ir} = 0 \tag{2}$$

$$T_{,t} + u_i T_{,i} = T_{,ii} + Q \tag{3}$$

where u is velocity, P is dynamic pressure, η is viscosity, Ra is the Rayleigh number (defined below), T is temperature, δ_{ij} is the Kronecker delta, Q is heat production rate, i and j represent spatial indices, r is a unit vector in the radial direction, t is time, and the form $X_{,j}$ represents the derivative of X with respect to y. Repeated indices imply summation. The governing equations (1)–(3) are solved using the finite element community code *CitcomS* (version 3.3, Moresi & Solomatov, 1998; Zhong et al., 2000, 2008).

The vigor of convection, as defined for pure basal convection, can be described by a Rayleigh number:

$$Ra = g\,\rho\,\alpha\,\Delta T d^3/(\kappa\eta) \tag{4}$$

where α is the thermal expansivity, ρ is the density, η_0 is the reference viscosity, ΔT is the reference temperature drop given as the temperature contrast from the convecting layer depth (d) to the surface

($T_b - T_s$), and g is the gravitational acceleration. The nondimensional quantity Q characterizes the internal heat generation rate:

$$Q = Hd^2/(\kappa\Delta T) \tag{5}$$

where H is the volumetric heating rate.

Variables are nondimensionalized following:

$$t = \frac{d^2}{\kappa}t' \qquad u = \frac{\kappa}{d}u' \qquad \eta = \frac{\kappa}{d}\eta' \qquad \Delta T = \Delta T T' \qquad q_{\text{conv}} = \frac{\kappa\Delta T}{d}Nu \qquad \tau = \frac{\eta_0\kappa}{d^2}\tau' \tag{6}$$

where κ is the thermal diffusivity, q_{conv} is the heat flux, Nu is the nondimensional heat flux, k is the thermal conductivity, and τ is the stress. Variables marked as X' are taken to be dimensionless in equation (6); primes are dropped for clarity elsewhere.

Viscosity is assumed temperature dependent as given by

$$\eta(T) = \eta_0 \exp\left(A\left[\frac{1}{T+1} - \frac{1}{2}\right]\right) \tag{7}$$

where the rheological parameter A is the nondimensional activation energy that controls the total variation in the temperature-dependent viscosity ($\Delta\eta$) of the system (it is implied the Ra is defined for a viscosity at $T = 0.5$). The internal temperature, despite cases with high Q values, falls within the boundary surface and basal temperatures [T_s, T_b] (e.g., $T < T_b$ for all cases). The reference viscosity (η_0) is controlled in part by the ice grain size (e.g., McKinnon, 2006). Despite ice grain sizes in the outer satellites being poorly constrained (e.g., Barr & McKinnon, 2007; Kirk & Stevenson, 1987), it has been suggested that a reasonable assumption of the dimensional reference viscosity of ice at the base of an ice shell to be $\eta_0 \sim 10^{13}$ to $\sim 10^{15}$ Pa·s (e.g., Durham & Stern, 2001; Pappalardo et al., 1998), which corresponds to an ice grain size range of 0.1–2 mm (e.g., Barr & McKinnon, 2007; Han et al., 2012; Kirk & Stevenson, 1987).

We have modified the boundary condition of *CitcomS* to allow for a smooth variation in surface temperature with colatitude φ in the functional form $\sin(\varphi)$, which allows for maximum insolation at the equator and minimum insolation at the pole (assuming an axial tilt of ~0° from the solar plane and a fixed bond albedo). Along the ice-ocean interface, the ice shell may reach ~273 K assuming a low salinity ocean (e.g., Glein et al., 2015), which we take as our basal thermal boundary condition ($T_b = 1$ nondimensionally, as per equation (5)). Variations in surface temperatures from pole to equator of airless bodies may be expected to be a few tens of Kelvins (e.g., Nadeau & McGehee, 2017; Ojakangas & Stevenson, 1989). We take this variation to be ~16% the temperature at the base of the ice shell, or equivalently 45 K as a maximum value, in line with, though slightly lower than, suggestions for the Galilean system (e.g., Nimmo & Manga, 2009; Ojakangas & Stevenson, 1989; Squyres, 1980). A subset of models is tested at half the surface temperature variation, ~8% the basal temperature or 22.5 K, in line with suggestions for the Saturnian and Uranian systems. Additional detail is given in the supporting information (Baland et al., 2016; Bergstralh et al., 1991; Howett et al., 2011; Murray & Dermott, 1999; Whitaker & Greenberg, 1973).

We run suites of numerical experiments for both homogeneous and latitudinally variable surface temperature conditions, under both isoviscous and temperature-dependent viscosity formulations. In addition to basally heated systems, a subset of mixed heating models with high degrees of internal heating is additionally explored in order to mimic the effects of tidal heating. Uniform internal heating rates range from a maximum value of $Q = 49$ to a minimum of $Q = 10$ (where $Q = 0$ represents basal heating conditions), which correspond roughly to $H \sim 10^{-10}$ to $\sim 10^{-11}$ W/kg, respectively (e.g., O'Neill & Nimmo, 2010), and are calculated using the average surface temperature following equation (5). We consider a range of Ra values estimated to be representative for the icy satellites: $3{\cdot}10^5$, $7{\cdot}10^5$, and $3{\cdot}10^6$, corresponding to a reference viscosity of O (10^{14}) Pa·s. For our nominal model space, we mostly focus on the lowest representative Ra ($3{\cdot}10^5$), with higher Ra values (more numerically intensive) limited to testing the robustness of our solution space. Table 1 illustrates how these model parameters are expected to compare to a set of satellites spanning, and largely representative of, three gas giant planetary systems (Jovian:Europa; Saturnian:Enceladus; and Uranian:Miranda).

Table 1
Model Parameter Comparison With Example Satellites

Name	Symbol	Satellite parameters			Units
		Europa	Enceladus	Miranda	
Dimensional quantities					
Surface gravity	g	1.315	0.111	0.083	m/s^2
Initial ice shell thickness	D	20–100	20–60	59–130	km
Satellite radius	R	1561	252	235.8	km
Surface temperature (pole-equator)	T_s	48–110	48–63	30–62	K
Ice density	ρ_i		950		kg/m^3
Thermal expansivity	α		$3{\cdot}10^{-5}$		K^{-1}
Basal temperature	T_b		273		K
Thermal diffusivity	κ		$1{\cdot}10^{-6}$		m^2/s
Basal viscosity	η		10^{13}–10^{15}		Pa s
Heat production	H		$1{\cdot}10^{-11}$–$2.3{\cdot}10^{-10}$		W/kg
Nondimensional quantities					
Estimated basal Rayleigh number (ice shell)	Ra	$1{\cdot}10^5$–$3{\cdot}10^7$	$2{\cdot}10^4$–$2{\cdot}10^7$	$3{\cdot}10^5$–$3{\cdot}10^8$	
Core fraction	f	0.94–0.99	0.76–0.92	0.45–0.75	
Surface temperature variation	ΔT_s	0.27	0.07	0.14	
Heat production (input)	Q		2–49		

Note. Satellite parameters are taken from Ojakangas and Stevenson (1989), Bergstralh et al. (1991), Schubert et al. (2007), Nimmo and Manga (2009), Spencer et al. (2009), Sotin et al. (2009), O'Neill and Nimmo (2010), Hammond and Barr (2014a), Quick and Marsh (2015), Beuthe et al. (2016), and references therein. Surface temperature variation calculations follow Ojakangas and Stevenson (1989), see supporting information. Estimates of *Ra* follow from equation (4) using estimated ranges for the reference viscosity of ice, the ice shell thickness, and surface and basal temperatures.

In order to isolate the effects of latitudinally variable surface temperatures on the planform of convection, both latitudinally variable and homogeneous surface temperature cases are run at the same average surface temperature (e.g., $T_s \approx 0.105$). That is, both models are designed to operate with approximately the same effective *Ra*, as defined by equation (6) using the average surface temperature. For models with temperature-dependent viscosities, the rheological parameter, A, is chosen to yield a variation in viscosity from the base of the domain to the surface of 10^2–$3{\cdot}10^4$. At high viscosity contrasts ($\Delta\eta \geq 10^4$), the system enters a characteristic stagnant lid regime where convection only occurs under a thick immobile lid. For both simplicity and to be consistent with previous studies, we adopt a Newtonian flow formulation (e.g., Han et al., 2012; O'Neill & Nimmo, 2010). The core fraction, or curvature, is defined as the ratio of the inner to outer boundaries ($f = R_i/R_0$). In our models this is set to 0.762, which gives a dimensionless ice shell thickness (d) of 0.238 (~24% of a general satellite radius). This would imply an ice shell thickness of ~ 60 km for a general Enceladus or Miranda type satellite, which is in the range for suggested current maximum Enceladian ($d \sim 60$ km) and minimum Mirandian ($d \sim 59$ km) ice shell thicknesses (see Table 1 and caption). Due to the overlapping ranges in key satellite parameters (e.g., R_i, g, T_s) and the assumed shell thickness of ~ 60 km, Enceladus and Miranda type satellites are, for our cases here (e.g., in terms of system behaviors and metrics such as surface/internal velocities), broadly similar. In the case of Europa, full 3D spherical shell experiments exploring currently expected ice shell geometries (f as great as 0.99; Table 1) are computationally demanding, and as a result this geometry is not explicitly considered. The model domains consist of $65 \times 65 \times 32$, $65 \times 65 \times 65$, or $129 \times 129 \times 65$ grid cell elements (x, y, and z directions, respectively) for each of the 12 spherical caps of *CitcomS'* mesh structure; higher resolutions are necessary to adequately resolve the velocity structure of both larger *Ra* and isoviscous models. As discussed in the supporting information, lower resolution models are not as well resolved and show small velocity artifacts. Boundary conditions are free slip. Each numerical experiment is run to a statistically steady state where the time-averaged heat flow from the surface is equal to within ~ 1% of the base. Isoviscous models were initialized from a conductive state with the same temperature perturbation of 0.1 magnitude in spherical harmonics degree three at mid-model depths. Following statistically steady state conditions for the isoviscous system, temperature-dependent viscosity is added. Simulations are run to a minimum of 20 overturn times (time a parcel takes to traverse the ice shell) to ensure that the system is sufficiently removed from its initial state (e.g., isoviscous flow structure). Additionally, select models with temperature-dependent viscosity were initialized from the

original conductive state and temperature perturbation to ensure that the results were not strongly influenced by the isoviscous initial condition. The results of 67 three-dimensional numerical experiments are summarized in Table 2.

3. Convection With Homogeneous and Latitudinally Variable Surface Temperatures

3.1. Basally Heated Isoviscous Systems

In order to isolate the effects of a pole to equator variation in T_s on the planform of convection, we initially consider simple isoviscous experiments. These models are driven by basal heating and are designed to operate at the same average surface temperature and approximately the same effective *Ra* (see supporting information). The basal *Ra* is fixed for each model at $3{\cdot}10^5$. For isoviscous convection, surface velocities have a simple relation to interior convection and mobility of the system (defined as $M = u_{\text{surface}}/u_{\text{mantle}}$). Mobility is a measure of the surface dynamics and the average level of interaction with the interior globally. In general, high mobilities, as for instance those here that approach unity, indicate that the surface moves at the same velocity as the interior of the convecting system; that is, the surface participates in and is the expression of the convecting cell at depth. Therefore, the surface dynamics are largely representative of the convecting system as a whole. In contrast, low mobilities, those less than unity and greater than ~0.1, indicate that the surface lags behind the convecting interior, though it may still participate in overturn and the convective cycle. For mobilities much less than ~0.1, the surface no longer participates in a meaningful way with the convecting interior.

As compared to a homogeneous T_s case, the net effect of a pole to equator variation in surface temperature is to disrupt the planform of convection. This can be seen clearly in the surface velocity plots (Figure 1). A homogeneous surface temperature favors large Rayleigh-Bénard style convective cells, with broad upwelling sites and ring-like downwelling curtains. Surface velocities have no preferred global orientation, instead they are strictly controlled by *local* upwelling and downwelling sites with little communication between stable cells, though they are coupled at their boundaries. As a result, both heat flow and strain rate are largely focused into a *patchwork* structure. Mobility for both surface temperature cases is ~1.2 (less than 2% difference between cases). Surface velocities for both cases are approximately 1,700 (nondimensional velocity u_s'), which leads to a dimensional velocity $u_s \sim 20$ cm/a, from equation (6) using the defined ice shell thickness (d) of 60 km. Stress (τ) can be calculated by multiplying the strain rate and viscosity fields with a factor of 2. The viscosity is uniform in isoviscous models, so stress also reflects the strain rate field. With a reference viscosity of 10^{14} Pa·s, the average and maximum dimensional surface stress is $\tau_{\text{mean}} \sim 1$ and $\tau_{\text{max}} \sim 16$ Pa ($\tau'_{\text{max}} \sim 580$, dimensionalized using equation (6)) for both surface temperature cases. All figures are snapshots at a single time in the statistically steady state simulations. Each result is checked to ensure that the global flow structures are representative through the simulation (quasi steady state).

The application of a variation in T_s (maximal at equator and minimal at the poles) results in a disruption of this configuration. The equatorial region tends to favor warm upwellings as indicated by a band of low velocities, high heat flows, and high strain rates in Figure 1, while downwellings tend to be concentrated in the polar region. The downwelling zones become elongated, hemispheric in scale, and oriented nearly perpendicular to the equator. This is reflected in the velocity field at the surface, where material is generally transported away from the warmer equator toward the cooler poles. This poleward oriented convective cell results in heat flow and velocity gradients that are focused along the equator and along lines of longitude toward the poles.

Heat flux (Figures 1b and 1e) is a proxy for age (flux is inversely proportional to the square root of cooling age for a half-space) and boundary layer (or *lithospheric*) thickness and can offer a window into the internal structure of the convective shell. Regions of high heat flow correspond to upwelling zones of higher internal temperatures, where low heat flow corresponds to regions of downwellings and lower internal temperatures. Consequently, the boundary layer thickness is controlled by the local upwelling and downwelling structure in the homogeneous T_s case and the variation in the global surface temperatures in the latitudinally variable T_s case. Here the boundary layer thins in warmer equatorial regions with active upwellings and thickens in the colder polar regions or active downwellings, preferentially (e.g., Figure 2).

Table 2
Convection Results

Ra_{shell}	Resolution	Homogeneous/ variable	T_s	$\Delta\eta$	Q_{input}	T_i	Mobility	RMS velocity	Nu_{surf}	Nu_{bot}	Misfit (%)	$l = 2$ (%)	Figure
$3\cdot10^5$	65 × 65 × 33	Homogeneous	0.000	10^0	0	0.35	1.17	1517.80	11.47	11.63	−1.45	—	—
$3\cdot10^5$	65 × 65 × 65	Homogeneous	0.000	10^0	0	0.36	1.17	1512.50	12.10	11.98	1.04	1.65	—
$3\cdot10^5$	129 × 129 × 65	Homogeneous	0.000	10^0	0	0.35	1.18	1514.00	12.26	12.24	0.18	1.25	—
$7\cdot10^5$	65 × 65 × 65	Homogeneous	0.052	10^0	0	0.41	1.14	2403.70	14.04	13.97	0.54	2.40	—
$7\cdot10^5$	65 × 65 × 65	Homogeneous	0.083	10^0	0	0.40	1.16	2416.10	14.20	14.13	0.49	1.43	9
$7\cdot10^5$	65 × 65 × 65	Variable	0.083	10^0	0	0.39	1.15	2435.00	14.46	14.46	−0.01	11.44	9
$7\cdot10^5$	65 × 65 × 65	Homogeneous	0.105	10^0	0	0.42	1.15	2371.50	13.55	13.53	0.18	0.24	7
$7\cdot10^5$	65 × 65 × 65	Variable	0.165	10^0	0	0.45	1.18	2292.70	12.81	12.72	0.76	16.01	7
$3\cdot10^6$	129 × 129 × 65	Homogeneous	0.520	10^0	0	0.40	1.11	6013.40	23.23	23.40	−0.76	1.16	—
$3\cdot10^6$	129 × 129 × 65	Variable	0.083	10^0	0	0.40	1.12	5839.70	22.62	22.76	−0.67	10.40	—
$3\cdot10^6$	129 × 129 × 65	Homogeneous	0.105	10^0	0	0.43	1.11	5768.70	21.60	21.75	−0.70	0.18	8
$3\cdot10^6$	65 × 65 × 65	Homogeneous	0.105	10^0	0	0.43	1.08	5606.30	20.81	20.68	0.64	3.37	—
$3\cdot10^6$	129 × 129 × 65	Variable	0.165	10^0	0	0.44	1.15	5239.20	19.86	19.90	−0.24	20.73	8
$3\cdot10^6$	65 × 65 × 65	Variable	0.165	10^0	0	0.44	1.09	4806.60	19.26	19.08	0.96	—	—
$3\cdot10^5$	65 × 65 × 33	Homogeneous	0.105	10^0	0	0.42	1.17	1421.70	10.03	10.12	−1.08	0.15	—
$3\cdot10^5$	65 × 65 × 65	Homogeneous	0.105	10^0	0	0.42	1.18	1413.10	10.33	10.26	0.71	3.01	1, 2
$3\cdot10^5$	129 × 129 × 65	Homogeneous	0.105	10^0	0	0.42	1.18	1414.90	10.52	10.53	−0.09	0.66	—
$3\cdot10^5$	65 × 65 × 33	Variable	0.165	10^0	0	0.45	1.20	1393.70	9.60	9.61	−0.15	—	—
$3\cdot10^5$	65 × 65 × 65	Variable	0.165	10^0	0	0.45	1.20	1386.50	9.93	9.85	0.82	17.24	1, 2
$3\cdot10^5$	65 × 65 × 33	Homogeneous	0.105	10^2	0	0.53	1.01	425.09	5.09	5.05	0.94	1.97	3a, 4a
$3\cdot10^5$	65 × 65 × 65	Homogeneous	0.105	10^2	0	0.54	1.01	428.37	5.07	5.05	0.50	—	—
$3\cdot10^5$	65 × 65 × 33	Variable	0.165	10^2	0	0.55	1.08	450.78	4.89	4.85	0.97	14.76	3b, 4a
$3\cdot10^5$	65 × 65 × 65	Variable	0.165	10^2	0	0.55	1.09	453.24	4.97	4.94	0.73	—	—
$3\cdot10^5$	65 × 65 × 33	Homogeneous	0.105	10^3	0	0.57	0.67	245.10	3.00	2.99	0.43	5.81	3a, 4b
$3\cdot10^5$	65 × 65 × 65	Homogeneous	0.105	10^3	0	0.58	0.71	251.17	3.04	3.03	0.34	—	—
$3\cdot10^5$	65 × 65 × 33	Variable	0.165	10^3	0	0.58	0.80	268.47	3.11	3.10	0.52	6.35	3b, 4b
$3\cdot10^5$	65 × 65 × 65	Variable	0.165	10^3	0	0.58	0.81	266.45	3.07	3.06	0.45	—	—
$3\cdot10^5$	65 × 65 × 33	Homogeneous	0.105	10^4	0	0.77	0.02	174.22	2.45	2.45	−0.14	0.27	3a, 4c
$3\cdot10^5$	65 × 65 × 65	Homogeneous	0.105	10^4	0	0.77	0.03	175.92	2.46	2.46	−0.47	—	—
$3\cdot10^5$	65 × 65 × 33	Variable	0.165	10^4	0	0.76	0.08	179.90	2.43	2.43	0.01	2.64	3b, 4c
$3\cdot10^5$	65 × 65 × 65	Variable	0.165	10^4	0	0.76	0.09	177.89	2.41	2.41	−0.11	—	—
$3\cdot10^6$	129 × 129 × 65	Variable	0.000	10^2	0	0.60	1.11	1760.23	10.43	10.39	0.42	17.76	10
$3\cdot10^6$	129 × 129 × 65	Homogeneous	0.000	10^2	0	0.60	1.05	1673.98	10.78	10.73	0.51	6.35	10
$3\cdot10^6$	129 × 129 × 65	Homogeneous	0.000	10^4	0	0.81	0.00	685.86	4.41	4.42	−0.36	3.46	—
$3\cdot10^6$	129 × 129 × 65	Homogeneous	0.052	$3\cdot10^4$	0	0.81	0.02	732.20	4.39	4.41	−0.68	0.58	—
$3\cdot10^6$	129 × 129 × 65	Homogeneous	0.105	$3\cdot10^4$	0	0.81	0.02	746.61	4.36	4.38	−0.48	0.74	—
$3\cdot10^6$	129 × 129 × 65	Variable	0.165	$3\cdot10^4$	0	0.81	0.06	761.46	4.39	4.40	−0.24	3.26	—
$3\cdot10^5$	65 × 65 × 33	Homogeneous	0.105	10^0	10	0.44	1.17	1418.50	10.43	9.90	−0.58	3.68	—
$3\cdot10^5$	65 × 65 × 33	Variable	0.165	10^0	10	0.47	1.19	1390.60	10.04	9.47	−0.14	—	—
$3\cdot10^5$	65 × 65 × 65	Variable	0.165	10^0	10	0.48	1.19	1373.00	10.26	9.58	1.07	13.80	—
$3\cdot10^5$	65 × 65 × 33	Homogeneous	0.105	10^2	10	0.58	1.08	466.44	5.27	4.65	0.96	4.89	—
$3\cdot10^5$	65 × 65 × 33	Variable	0.165	10^2	10	0.58	1.12	480.57	5.20	4.57	1.01	16.53	—
$3\cdot10^5$	65 × 65 × 33	Homogeneous	0.105	10^3	10	0.63	0.70	267.53	3.44	2.85	0.37	0.84	—
$3\cdot10^5$	65 × 65 × 33	Variable	0.165	10^3	10	0.64	0.88	305.80	3.49	2.90	0.60	3.28	—
$3\cdot10^5$	65 × 65 × 33	Homogeneous	0.105	10^4	10	0.81	0.02	188.01	2.75	2.17	−0.28	0.25	—
$3\cdot10^5$	65 × 65 × 33	Variable	0.165	10^4	10	0.81	0.06	192.37	2.75	2.18	−0.26	3.63	—
$3\cdot10^5$	65 × 65 × 33	Homogeneous	0.105	10^0	25	0.48	1.15	1381.50	10.99	9.56	−0.18	—	—
$3\cdot10^5$	65 × 65 × 65	Homogeneous	0.105	10^0	25	0.49	1.15	1368.30	11.53	10.00	0.69	0.18	—
$3\cdot10^5$	65 × 65 × 33	Variable	0.165	10^0	25	0.50	1.17	1356.30	10.66	9.17	0.39	—	—
$3\cdot10^5$	65 × 65 × 65	Variable	0.165	10^0	25	0.56	1.13	1252.50	10.89	9.43	0.12	—	—
$3\cdot10^5$	65 × 65 × 33	Homogeneous	0.105	10^2	25	0.65	1.15	524.64	5.76	4.27	0.76	1.41	—
$3\cdot10^5$	65 × 65 × 33	Variable	0.165	10^2	25	0.65	1.17	542.18	5.74	4.25	0.73	19.54	—
$3\cdot10^5$	65 × 65 × 33	Homogeneous	0.105	10^3	25	0.70	0.99	350.01	3.87	2.41	0.30	0.89	—
$3\cdot10^5$	65 × 65 × 33	Variable	0.165	10^3	25	0.70	1.02	366.21	3.97	2.50	0.42	8.38	—
$3\cdot10^5$	65 × 65 × 33	Homogeneous	0.105	10^4	25	0.87	0.02	195.93	3.13	1.69	−0.44	0.19	—
$3\cdot10^5$	65 × 65 × 33	Variable	0.165	10^4	25	0.88	0.08	203.11	3.14	1.69	−0.43	5.29	—
$3\cdot10^5$	65 × 65 × 33	Homogeneous	0.105	10^0	49	0.55	1.09	1269.20	12.28	9.30	1.22	—	—
$3\cdot10^5$	65 × 65 × 65	Homogeneous	0.105	10^0	49	0.55	1.08	1248.30	12.64	9.69	0.84	0.39	5
$3\cdot10^5$	65 × 65 × 33	Variable	0.165	10^0	49	0.57	1.11	1257.00	11.78	8.81	1.16	—	—

Table 2
(continued)

Ra_{shell}	Resolution	Homogeneous/ variable	T_s	$\Delta\eta$	Q_{input}	T_i	Mobility	RMS velocity	Nu_{surf}	Nu_{bot}	Misfit (%)	$l = 2$ (%)	Figure
$3{\cdot}10^5$	65 × 65 × 65	Variable	0.165	10^0	49	0.57	1.11	1242.20	12.07	9.11	1.01	11.18	5
$3{\cdot}10^5$	65 × 65 × 65	Homogeneous	0.105	10^2	49	0.74	1.21	595.07	6.48	3.63	0.05	23.18	—
$3{\cdot}10^5$	65 × 65 × 65	Variable	0.165	10^2	49	0.73	1.22	597.25	6.49	3.64	0.15	39.40	—
$3{\cdot}10^5$	65 × 65 × 65	Homogeneous	0.105	10^3	49	0.79	1.10	426.11	4.75	1.90	0.06	6.56	6
$3{\cdot}10^5$	65 × 65 × 65	Variable	0.165	10^3	49	0.79	1.16	453.41	4.85	2.00	0.11	7.12	6
$3{\cdot}10^5$	65 × 65 × 65	Homogeneous	0.105	10^4	49	0.96	0.02	196.92	3.77	0.96	−1.22	0.15	—
$3{\cdot}10^5$	65 × 65 × 65	Variable	0.165	10^4	49	0.96	0.10	205.95	3.72	0.90	−1.04	7.51	—

Note. $\Delta\eta$ is the temperature-dependent viscosity contrast of the system. The Rayleigh number, *Ra*, is defined for domain of the ice shell, and internal heating *Q* is defined as the input parameter. Resolutions are given per spherical cap in the *X*, *Y*, and *Z* directions, respectively (where *Z* is the radial direction). The temperature and root-mean-square (RMS) velocity structure within the shell are computed from both horizontal and time averages of the internal temperature and velocity fields. Mobility is the ratio of surface to bulk internal velocity (see text). Heat flow from the surface and the base of the domain are given as Nusselt numbers. The misfit, reported as the percent difference, between the surface and basal heat flux is a measure of the balance in global heat flow. Higher misfits indicate less resolved models. The ratio of the $l = 2$, $m = 0$ component of the poloidal power spectrum is given as a percent of the entire poloidal power spectrum. All values are nondimensional.

Figure 2 illustrates the meridionally averaged variation in internal structure from pole to equator (marked as *eq*) for the convective shells. Results are further time averaged across statistically steady state solutions (minimum of 1.5 overturn times). Equatorial ice of the latitudinally variable T_s case is indeed warmer, with a thinner boundary layer, and the poles are significantly colder with thicker boundary layers (Figures 2c and 2d). The net motion of the surface is also shown to be directed poleward (Figure 2b). The thermal boundary layer depth from the surface (z_{TBL}) is calculated from the inflection point of the second derivative of the meridionally averaged radial temperature field, which corresponds to the transition from conductive to convective profiles (consistent with the approach of Moore, 2008; Weller et al., 2016). Select profiles were additionally tested using both the horizontal velocity field (10% of bulk internal velocity defining the base of the mechanical *lithosphere*) and classic boundary layer/heatflow scaling relationships (e.g., Turcotte & Schubert, 2005). All approaches calculated the z_{TBL} to be in ~1% of each other. The z_{TBL} is calculated as a

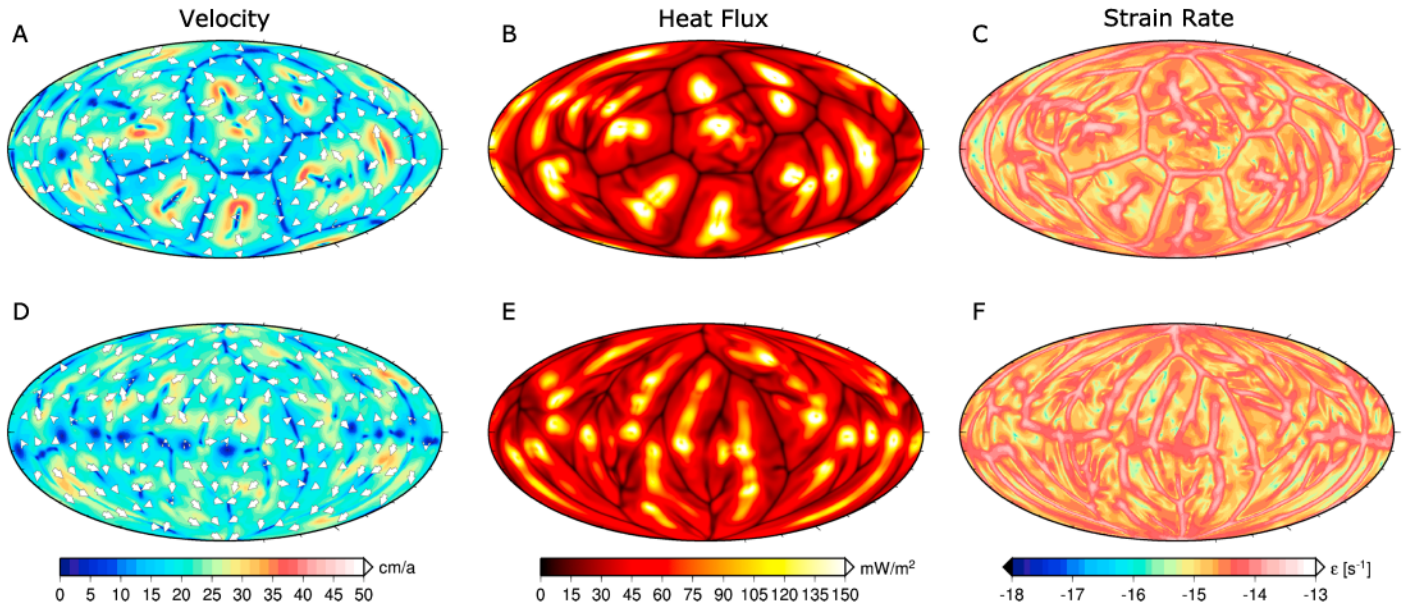

Figure 1. Basal heating isoviscous results for homogeneous (top row) and latitudinally variable (bottom row) surface temperatures. Plots show surface velocity field (a, d), heat flux (b, e), and strain rate (c, f). The basal *Ra* is fixed at $3{\cdot}10^5$, and the average surface temperatures are identical. Arrows denote surface flow direction. Quantities are dimensionalized following equation (6), using $d = 60$ km, $\eta_0 = 10^{14}$ Pa·s, $\kappa = 10^{-6}$ m^2/s, and dimensionless quantities from selected models given in Table 2.

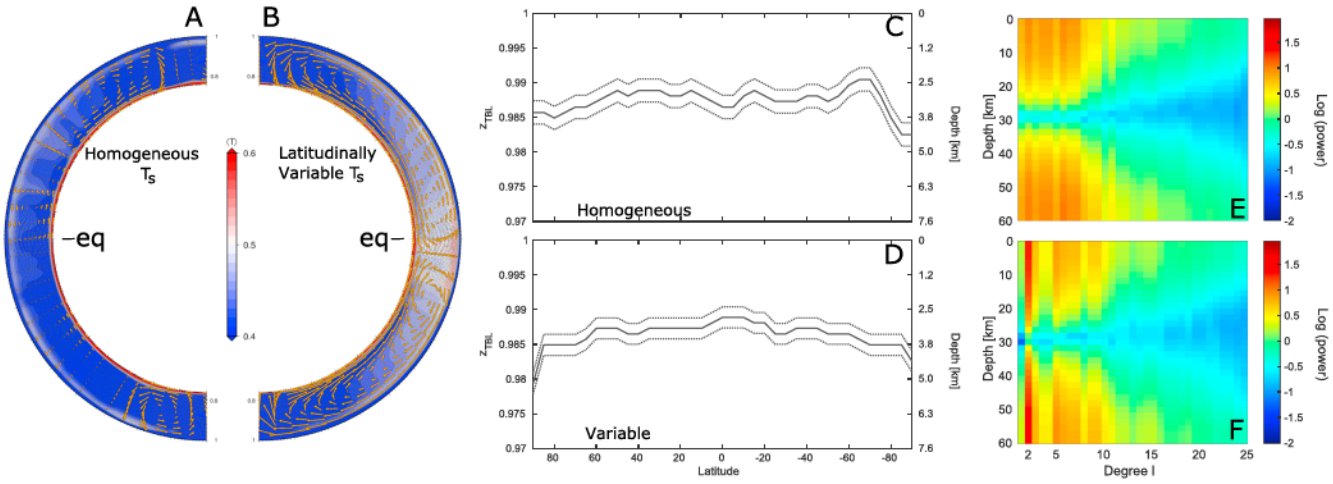

Figure 2. Meridionally and temporally averaged internal temperature and velocity plots for homogeneous (a) and latitudinally variable (b) surface temperatures for the basally heated isoviscous models shown in Figure 1. Colorbar for dimensionless temperatures are clipped at 0.4 to 0.6 to emphasize internal variations. Arrows denote average flow direction and magnitudes (minimum and maximum velocities are 0.2 and 38 cm/a, respectively). The equator is marked by *eq*; radius ranges from 0.762 to 1. Thermal boundary layer depths and thicknesses (see text) are shown for the homogeneous (c) and latitudinally variable (d) T_s cases. Solid lines are the mean, and dashed lines denote one standard deviation for the temporally and latitudinally averaged plots. Positive latitudes correspond to the top of the temperature slice. The log of the poloidal power spectra is shown for the homogeneous (e) and latitudinally variable (f) T_s cases. Quantities are dimensionalized following equation (6) with property values denoted in the Figure 1 caption.

function of latitude in 0.25° intervals to resolve small-scale features. The average z_{TBL} for both T_s cases is 0.987 (3.3-km thickness). The nondimensional radius of the outer surface (R_0) is set to 1, such that the nondimensional thickness of the convecting layer is given as $1 - R_i$ (outer minus inner radius). Dimensionalizing by the satellite radius (Table 1) results in the z_{TBL} thickness reported (given the similar values between the radii of Enceladus and Miranda, we report thicknesses based on Enceladus' radius). The standard deviation of the z_{TBL}, calculated over both the time and latitudinal domains, is 0.002 (0.5 km). An inspection of the homogenous T_s case in Figure 2c indicates an asymmetric z_{TBL} about the pole. A global minima in depth occurs at ~ 70°S and a global depth maxima occurs at the south pole, apparently similar to the variable T_s case. The z_{TBL} thickness minima and maxima, as well as its gradient, offer clues to resolve the apparent discrepancy. The variable T_s indicates global minima and maxima at the poles and equator, with a steady (within natural variation) deepening of the z_{TBL} toward the poles. In contrast, the variation for the homogenous case from 70°S is not reflected globally, that is, the steep gradient is localized in extent. These suggest that this change in z_{TBL} is reflective of asymmetric convection, which is common within this *Ra* parameter range (e.g., Schubert et al., 2001).

The effect of variable insolation on these systems is then to break the asymmetric planforms that develop in favor of symmetry about the equator. This can be seen in greater detail in the averaged flow field (denoted by arrows). The homogeneous T_s case shows multiple convective cells operating in each hemisphere, with the equator being a zone of weak downwelling between two adjacent cells. The specific locations of upwelling and downwelling zones are arbitrary, and no one specific orientation would be preferred. The latitudinally variable T_s case shows two distinct, hemispheric-scale convective cells with poleward flow at the surface, and equatorward flow at the base, indicating a preferred orientation and symmetry due to variable surface temperature conditions in contrast to the constant case (see the z_{TBL}). Quantitatively, this is shown in the power spectra (Figures 2e and 2f), where the wavelengths of convection are obtained from the spherical harmonics decompositions of the poloidal velocity field at each radial level indicated up to spherical harmonic degree $l = 25$ (normalization of Dahlen & Tromp, 1998). Low l values indicate large wavelength features, with increasing l values corresponding to progressively smaller features. Due to the hemispheric symmetry imposed by the latitudinal variation in surface temperatures, we use the $l = 2$, $m = 0$ component of the poloidal velocities as a diagnostic metric of the power of the hemispheric-scale flow field (including higher-order m increases the power of the $l = 2$ component but otherwise does not qualitatively change these results). The dominant powers of the homogenous T_s case are spread fairly evenly between $l = 1$ and ~7. All degrees show a significant drop in power at the middepth, which corresponds to the velocity minima at the center of the

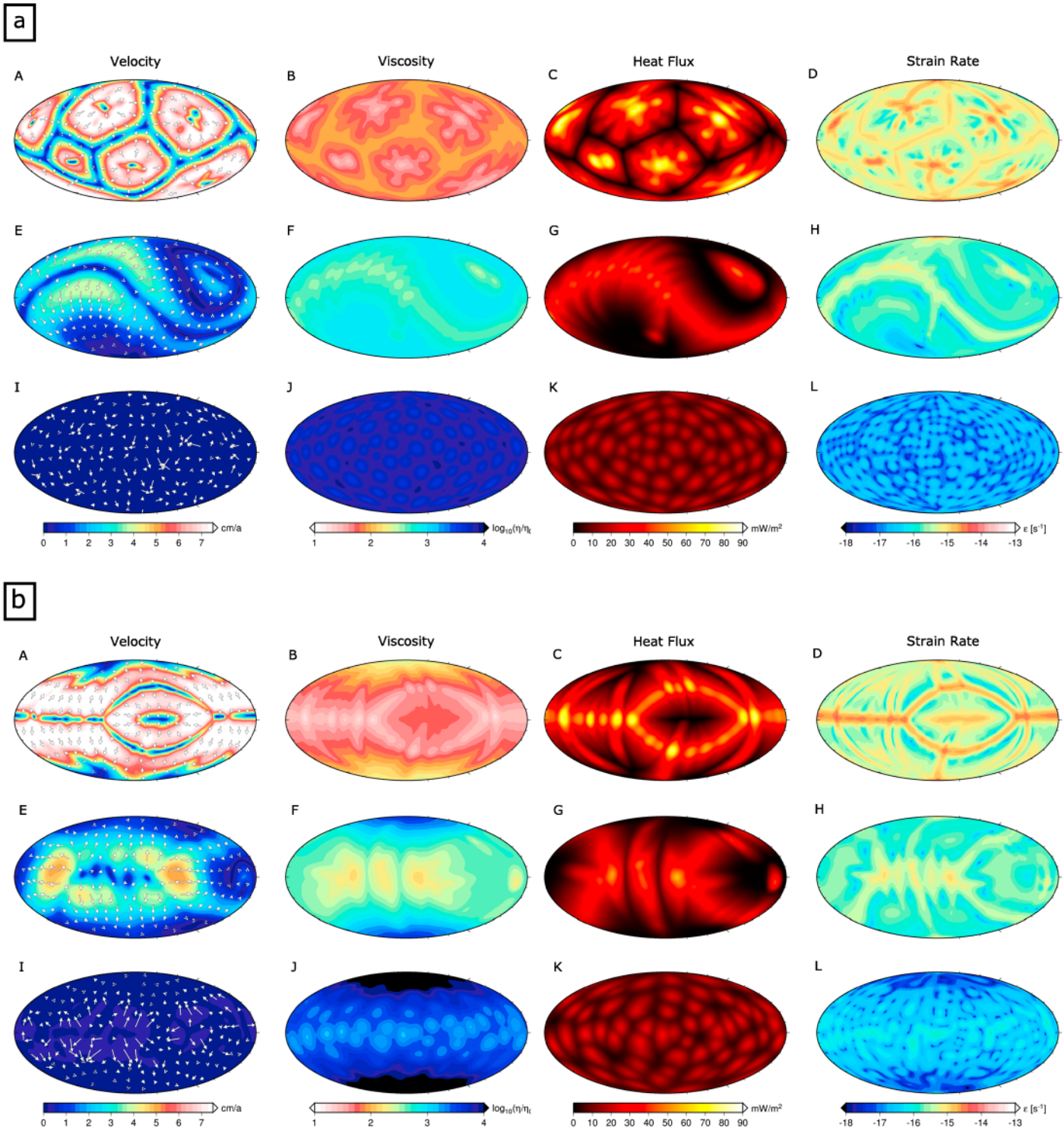

Figure 3. Basal heating temperature-dependent results for homogeneous (a) and latitudinally variable (b) surface temperatures. Plots show surface velocity field (A, E, I), surface viscosity (B, F, J), heat flux (C, G, K), and strain rate (D, H, L) for $\Delta\eta = 10^2$ (top row), 10^3 (middle row), and 10^4 (bottom row). The basal *Ra* is fixed at $3{\cdot}10^5$, and the model average surface temperatures are the same. Arrows denote surface flow direction. Quantities are dimensionalized following equation (6). Quantities are dimensionalized following equation (6) with property values denoted in the Figure 1 caption. Note for clarity that the scales for temperature-dependence differ from the isoviscous cases.

convective cells (Figures 2a and 2b). In contrast to the homogenous T_s case, the variable T_s case shows a significantly stronger maximum power for most depths at $l = 2$, with a much smaller power at $l = 3$ and 5–7, 9. While the homogenous T_s case does exhibit a moderately strong $l = 2$ power, the principle difference between the two cases is that the homogenous T_s case's power spectrum is spread across a wide range of l. For the variable T_s case, most power is at $l = 2$ for nearly all depths, consistent with the surface results of Figure 1 and the internal analyses of Figures 2a–2d. The velocity field in Figure 1d (indicated by arrow directions), which is not strongly oriented toward the poles (oriented instead toward smaller local downwellings), is reflective of the higher-order l seen in Figure 2f. The sum of the $l = 2$ power versus the sum of the total power spectrum further shows the distinct difference between the cases. The total $l = 2$ power in the variable T_s case is 17% of the total power in the convecting system versus the total power in $l = 2$ limited to ~3% of the total power for the homogenous T_s case. Due to the $l = 2$ flow structure in the variable T_s case, the majority of the mid-ice shell is isolated from the surface and basal flow (velocity minima internal to the convective cells).

3.2. Basally Heated Systems With Temperature-Dependent Viscosity

When temperature-dependent viscosity is introduced, overall surface velocities become more sluggish and the surfaces become increasingly isolated from the convective interior. We explore surface to basal (maximum temperature range) viscosity ratios ($\Delta\eta$) from 10^2 to 10^4 for both homogeneous and variable T_s scenarios. As viscosity contrasts increase, the global effective Ra (as defined in section 2) decreases by as much as an order of magnitude (e.g., Guerrero et al., 2018). In addition, velocity, mobility, and heat flux all decrease while internal temperature increases (Table 2). We focus on the large-scale global flow orientations as these are robust between model spaces.

Next, we explore the effects of latitudinally variable surface temperatures on more complex temperature-dependent viscosity systems. Figure 3a (homogeneous T_s) indicates that convective cells and the planform of convection tend to increase in spatial extent with increasing surface viscosity ($\Delta\eta < 10^4$). For a low viscosity contrast ($\Delta\eta = 10^2$, Figure 3a, panels A–D), the Rayleigh-Bénard style cells from Figure 1 increase in scale, and, as a result, vertical transport and surface deformation become localized (fewer but larger cells). Similarly, heat flux and strain rate become more localized, though at lower overall values compared to the isoviscous results. Surface velocity directions remain controlled by the numerous local upwelling and downwelling sites. As the surface viscosity increases ($\Delta\eta = 10^3$, Figure 3a, panels E–H), a large undulating upwelling forms in the lower latitudes, with a smaller more localized upwelling in the middle to upper latitudes. Heat flux and strain rate become further localized. In contrast to other homogeneous T_s cases, there is a strongly asymmetric global flow field with preferred orientations (single polar downwelling zones).

The effects of latitudinally variable T_s on temperature-dependent viscosity systems are striking (Figure 3b). For small viscosity contrasts ($\Delta\eta = 10^2$, Figure 3b, panels A–D), the Rayleigh-Bénard cells are disrupted, and the system instead favors localization and large-scale convective flow patterns that are stable in time; that is, the flow patterns are fixed spatially and temporally once they become established. Upwelling zones are favored along the region of maximal surface temperatures (the equator), and concentrated zones of downwellings occur along the region of lowest surface temperature (the poles). The midlatitudes are regions of maximum horizontal (surface) velocities, though high strain rates still are predominantly focused at the equator and poles. Due to the gradient in surface temperatures, surface viscosity varies from an equatorial low to a polar high with the midlatitude representative of the average value (coinciding with the average surface temperature). Mobility begins to diverge between the models ($\Delta\eta = 10^2$) and is ~1.01 and ~1.09 for the homogeneous and latitudinally variable T_s cases, respectively. These mobility values translate to average surface velocities of 435 (4.96 cm/a) and 496 (5.68 cm/a), for the homogeneous and latitudinally variable T_s cases, respectively. The difference of less than 8% between cases is relatively small but still greater than the natural variability within the system (~ 5%). Interestingly, the stresses at the surface show greater divergence than the previously discussed velocities ($\Delta\eta = 10^2$) or the results from the isoviscous cases. Stress averages are τ_{mean} ~ 0.01 and ~ 0.02 kPa, and stress maxima significantly increase from the isoviscous cases with τ_{max} ~ 0.28 and ~ 0.55 kPa for the homogeneous and latitudinally variable T_s cases, respectively (due to the increase in stress from isoviscous conditions, temperature-dependent cases will be reported in kilopascal). Average surface stresses increase, despite decreasing strain rates, due to a larger increase in viscosity globally. The maxima reflect stress localization into discrete zones of deformation, and as such can be

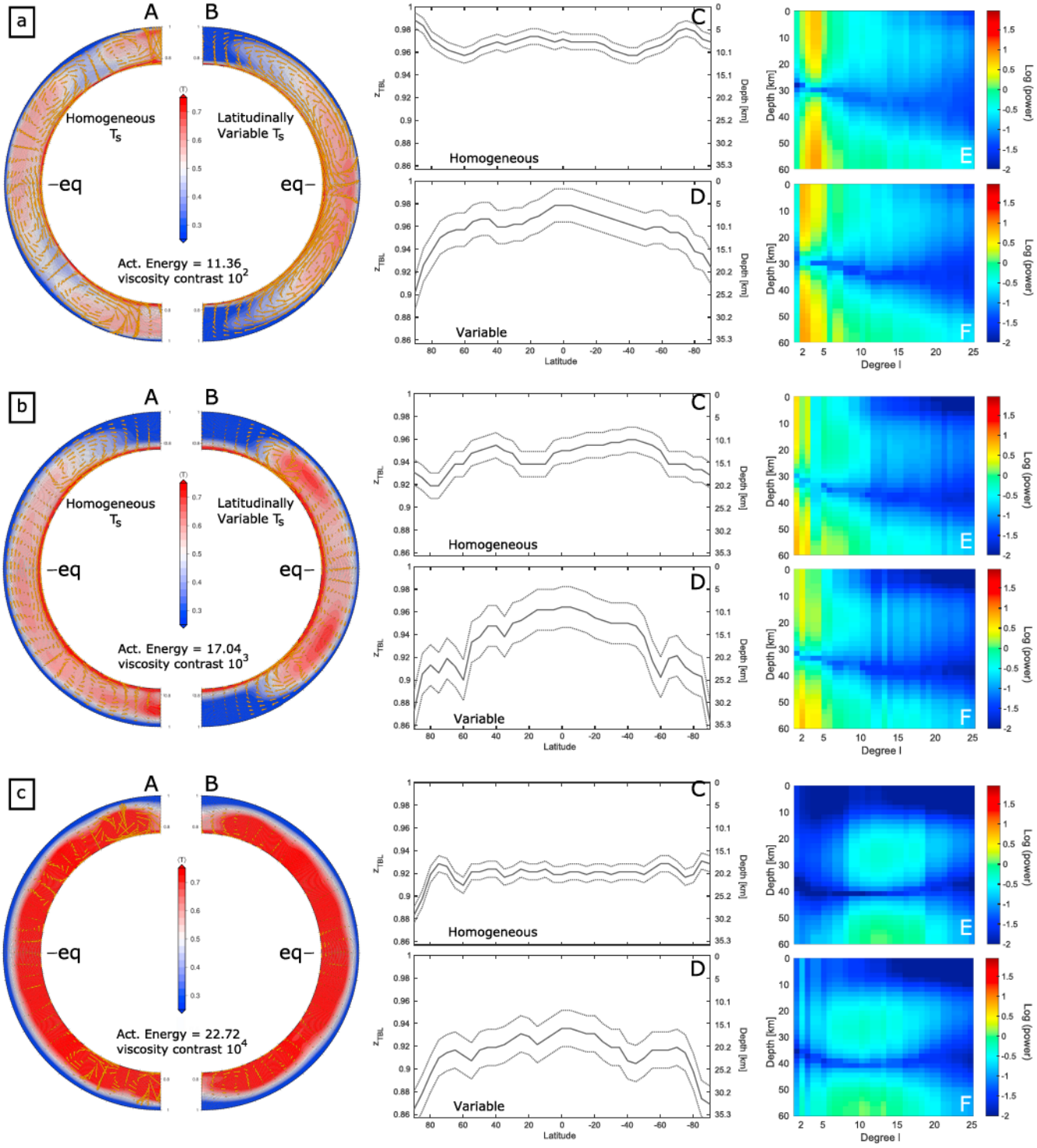

Figure 4. Meridionally and temporally averaged internal temperature and velocity plots for homogeneous (A) and latitudinally variable (B) surface temperatures for the basally heated temperature-dependent viscosity results shown in Figures 3a and 3b (a: $\Delta\eta = 10^2$; b: $\Delta\eta = 10^3$; c: $\Delta\eta = 10^4$). Positive latitudes correspond to the top of the temperature slice. Colorbar for temperatures are clipped at 0.25 to 0.75 to emphasize internal variations. Arrows denote average flow direction and magnitudes ($\Delta\eta = 10^2$ min / max velocities are 0.02 / 9 cm/a; $\Delta\eta = 10^3$ min/max velocities are 0.003 / 3 cm/a; and $\Delta\eta = 10^4$ min/max velocities are 10^{-4} / 2 cm/a). The equator is marked by *eq*. The radius ranges from 0.762 to 1. Boundary layer depths and thicknesses (see text) are shown for homogeneous (C) and latitudinally variable (D) cases. Solid lines are the mean, and dashed lines denote one standard deviation for the temporally and latitudinally averaged plots. The log of the poloidal power spectra are shown for the homogeneous (E) and latitudinally variable (F) cases. Quantities are dimensionalized following equation (6) with property values denoted in the Figure 1 caption.

considered a local instead of global process, and as a consequence can have values that far exceed the global average. In the homogenous surface temperature case, this occurs along the patchwork of downwelling zones (high viscosity and high strain rates) and in the center of the upwelling zones (low viscosity and maximum strain rates), as shown in Figure 3a, panels A–D. In the variable surface temperature case maximum viscosities occur in the middle to polar latitudes (with high strain rates), and maximum strain rates occur along polar upwelling bands (with low viscosity), consequently strain maxima occur in polar regions and along the equator (Figure 3b, panels A–D).

As the surface viscosity increases ($\Delta\eta = 10^3$, Figure 3b, panels E–H), heat flux and surface velocities decrease with decreasing effective *Ra*. Upwelling zones still occur near the equator; however, downwelling regions become pronounced, forming perpendicular to the equator and separating regions of upwellings. This can be seen by the three distinct upwelling zones, surrounded by downwelling sheets focused along the equator in the heat flux plot of Figure 3b (panel G). Mobility decreases substantially for both surface temperature cases, with values of ~0.8 and ~0.7 for the homogeneous and latitudinally variable T_s cases, respectively. Average surface velocities are 164 (1.87 cm/a) and 214 (2.44 cm/a) for the homogeneous and latitudinally variable T_s cases, respectively. Average surface stresses increase due to increasing viscosity to τ_{mean} ~ 0.03 and ~ 0.06 kPa, while maxima reach values of τ_{max} ~ 1.69 and ~ 2.35 kPa for the homogeneous and latitudinally variable T_s cases, respectively. Similar to the previous cases, stress is focused in a nonpreferred orientation associated with upwellings and downwellings in the homogeneous case, and along the poles and equator in the latitudinally variable case.

At high viscosity contrasts ($\Delta\eta \geq 10^4$), the system enters a different regime that of the stagnant lid (e.g., shown in Figure 3a, panels I–L). Here we define a stagnant lid at mobilities <0.1 with no surface participation in mantle overturn. Due to the variation in viscosity contrast from the latitudinally variable surface temperatures, the equatorial region is slightly less viscous than the poles ($\Delta\eta = 10^4$ is defined at the midlatitudes). This allows for small-scale surface motions that are orientated poleward, and consequently greater strain rates focused on the equatorial to midlatitude regions (Figure 3b, panels I–L). Additionally, warm upwelling plumes tend to not only be focused near the equator but also are enhanced in size and in surface heat flux from the homogeneous T_s case. Mobility drops to ~0.03 and ~0.09 for the homogeneous and latitudinally variable T_s cases, respectively, where the higher mobility reflects the enhanced surface velocity field nearly centered on the reduced viscosity equator. This corresponds to 4.32 (0.04 cm/a) and 16.01 (0.18 cm/a) for the homogeneous and latitudinally variable T_s cases, respectively. Both average and maximum surface stresses decrease to τ_{mean} ~ 0.02 and τ_{max} ~ 0.18 kPa for the homogeneous surface temperature case due to the cessation of appreciable surface velocities. However, while average stresses decrease to τ_{mean} ~ 0.04 kPa maximum surface stresses remain appreciably large at ~ 0.95 kPa for the latitudinally variable T_s case due to the local movement of the surface (Figure 3b).

The meridionally and temporally averaged internal structure of these temperature-dependent viscosity cases is shown in Figures 4a–4c. Similar to the isoviscous cases (Figure 2), the internal structure for the low viscosity contrast ($\Delta\eta = 10^2$) regime indicates that the latitudinally variable T_s case operates in hemispheric-scale convective cells, pinned to the equator and the poles (Figure 4a, panels A and B). Compared with the analogous homogeneous T_s case, the polar boundary layers are significantly thicker and the equatorial boundary layer is thinner. The average z_{TBL} (boundary layer depths) is 0.97 (8.0-km thick) and 0.96 (10.3-km thick), with standard deviations of 0.003 (0.75 km) and 0.02 (3.8 km) for the homogeneous and variable cases, respectively (Figure 4a, panels C and D). The power spectrum of the homogenous T_s case is spread between $l = 2$ and 5, with a $l = 4$ dominance, and a secondary $l = 3$ signal (Figure 4a, panel E). Similar to the isoviscous results, latitudinally variable T_s shifts the dominant power to lower degree (higher wavelength) with a significantly stronger (maximum power) signal at $l = 2$ and a secondary signal at $l = 3$ and 4 (Figure 4a, panel F). The ratio of total $l = 2$ power to the total power of the convective system decreases from the isoviscous case for both systems, with 2% and 15% for the homogeneous and latitudinally variable T_s cases, respectively. For the higher surface viscosity case of $\Delta\eta = 10^3$ (Figure 4b), the homogeneous T_s case exhibits strong asymmetry between polar flow features (upwelling and downwelling poles), while the latitudinally variable T_s case has symmetric polar downwelling zones with broader and thicker boundary layers. The z_{TBL} is 0.94 (14.1-km thick) and 0.95 (13.6-km thick), with standard deviations of 0.011 (2.7 km) and 0.024 (6.0 km), for the homogeneous and variable cases, respectively (Figure 4b, panels C and D). The

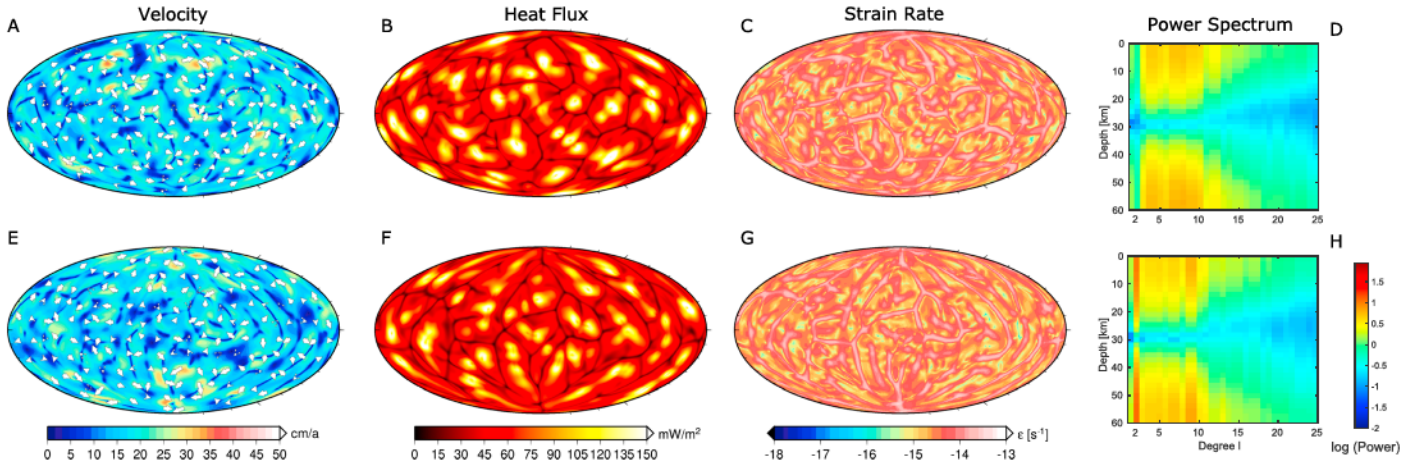

Figure 5. Mixed heating results with uniform viscosity for homogeneous (top row) and latitudinally variable (bottom row) surface temperatures. Plots show surface velocity field (a, e), heat flux (b, f), strain rate (c, g), and the log of the poloidal power spectra (d, h). The basal *Ra* is fixed at $3{\cdot}10^5$, and the average surface temperatures in both models are the same. Arrows denote surface flow direction. Quantities are dimensionalized following equation (6) with property values denoted in the Figure 1 caption.

power spectrum of the homogenous T_s case diverges from previous viscosity case results and is spread between $l = 1$ and 3, where $l = 1$ is dominant in this system. There is moderate power in both $l = 2$ and 3, with limited power in $l = 4$ and 6 (Figure 4b, panel E). Intermediate viscosity contrasts ($\Delta\eta = 10^3$) at *Ra* $O(10^5$–$10^6)$ and internal temperatures (~ 0.7 nondimensional or greater) favor long wavelength degree-1 type convective cells (McNamara & Zhong, 2005). In the case of the latitudinally variable T_s case, the maximum power still occurs at $l = 2$. However, now there is a much greater spread in total power, between $l = 1$ and 4, with an appreciable amount of power also in $l = 1$ (Figure 4b, panel F). Variable surface temperatures in previous cases (isoviscous and $\Delta\eta = 10^2$) caused the flow field to have more power in lower degrees compared to the analogous constant surface temperature cases. Here variable surface temperatures act to disrupt a preferred degree-1 structure in favor of higher degree convection, driving the systems slightly toward $l = 2$ due to the imposed thermal boundary condition while maintaining power in both $l = 1$ and higher degrees, which was not seen in previous examples. The ratio of total $l = 2$ power to the total power of the convective system is similar in both cases at ~ 6%. Though the latitudinally variable T_s case contains ~ 10% more power than the homogenous case. This thermal configuration resembles the effectively low Rayleigh number non-Newtonian grain size-dependent computations of Rozel et al. (2014), albeit focused along the equator due to the surface temperature gradient, as opposed to their pole-located plume. This indicates that an appropriately defined effective Rayleigh number may capture both cases, where *Rozel et al.*'s variations are due to locally higher mantle viscosity, and ours are due to temperature contrast variations.

At high viscosity contrasts ($\Delta\eta \geq 10^4$) in the stagnant lid regime (Figure 4c), internal velocities drop significantly. Boundary layers thicken and, as found for the less viscous cases, asymmetry that is prevalent for homogeneous T_s in flow and boundary layer thicknesses near the poles does not exist for the latitudinally variable T_s case. The average z_{TBL} is 0.93 (19-km thick) and 0.92 (20-km thick), and standard deviations are 0.0003 (0.08 km) and 0.017 (4.3 km) for the homogeneous and variable T_s cases, respectively (Figure 4c, panels C and D). The standard deviations for the variable surface temperature cases are notably larger than their homogenous counterparts. Since both T_s conditions are designed to operate at the same average surface temperature, the average z_{TBL} should be similar if not the same (as is the case for the isoviscous systems). The variable T_s cases then will have greater variability due to the insolation structure *imposed* at the boundary, which is reflected in the larger standard deviations.

The power spectrum of the homogenous T_s case shows a significant spread in power between $l = 8$ and 18, where $l = 12$ is dominant (Figure 4c, panel E). These values suggest small wavelength convection that is consistent with local scale drips and plumes impinging the thermal boundary layer (which is reflected in both the small standard deviation of the z_{TBL} and the smaller localized [plume] hot spots on the heat flux map in

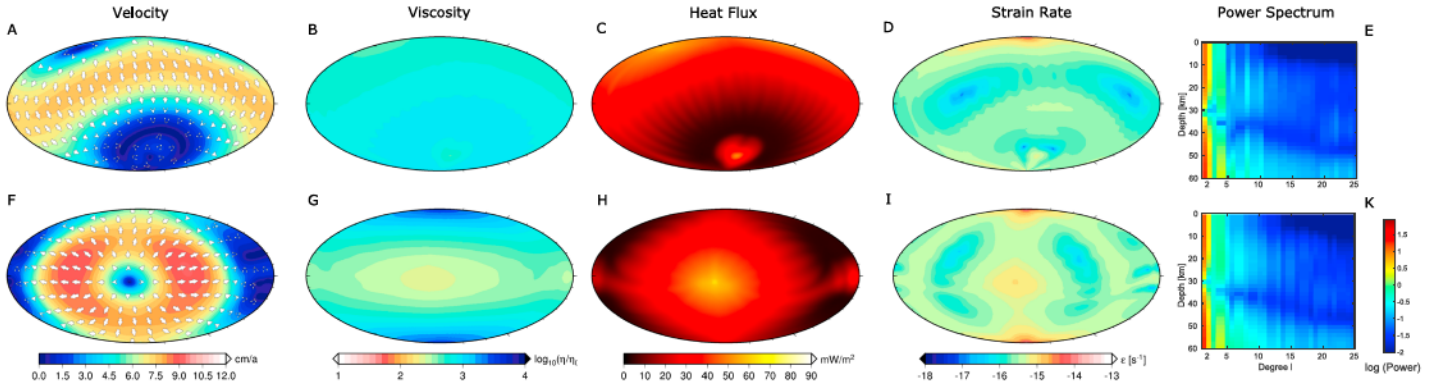

Figure 6. Mixed heating results with temperature-dependent viscosity for homogeneous (top row) and latitudinally variable (bottom row) surface temperatures. Plots show surface velocity field (a, f), surface viscosity (b, g), heat flux (c, h), strain rate (d, i), and the log of the poloidal power spectra (e, j) for $\Delta\eta = 10^3$. The basal Ra is fixed at $3{\cdot}10^5$, and the average surface temperatures for each model are the same. Arrows denote surface flow direction. Quantities are dimensionalized following equation (6) with property values denoted in the Figure 1 caption. Note for clarity that the scales for temperature dependence differ from the isoviscous cases.

Figure 3a, panel K). The variable surface temperature case is markedly different. A bifurcation of the power spectra occurs, with a strong $l = 2$ component and a spread in appreciable powers from $l = 4$ to 16. Even though the $l = 2$ is not dominant here, it is still present and reflective of the surface temperature condition. The ratio of total $l = 2$ power to the total power of the convective system decreases from the $\Delta\eta = 10^3$ case, with almost no power in the homogeneous T_s case and 3% in the latitudinally variable T_s case. The presence of the $l = 2$ power at depth and separately in the lid suggests that the lid and interior are both affected by the surface temperature condition, though differently, driving differential motions in between them. Velocity maxima exist at depth near the thick polar boundary layers and adjacent upper latitude cells. Throughout the remainder of the interior, velocities remain relatively low. This, in conjunction with high internal temperatures, indicates that despite stagnant lid behavior (i.e., no interaction from the deep interior to the surface), a pole to equator variation in surface temperatures can affect the interior.

3.3. Sensitivity to Changes in Parameters and Increasing System Complexity: Internal Heating, Vigor of Convection, and Surface Temperatures

Next, we test the effects of latitudinally variable surface temperatures on mixed heating systems with a high degree of internal heating (Q), increasing vigor of convection (Ra), and a reduction in the surface temperature variation to $T_s \sim 8\%$ at the base of the ice shell.

First, we consider systems with a high degree of internal heating to mimic the general effects of tidal heating. For comparison with the results from section 3.1, we choose an example isoviscous system with a basal $Ra = 3{\cdot}10^5$ and $Q = 49$. Surface velocities are generally more variable in their orientations as compared to the pure basal heating case, though while somewhat muted, an overall poleward orientation is still evident in the latitudinal surface temperature case (Figures 5a and 5e). In general, increased internal heating moves an isoviscous system to smaller aspect ratio cells (Schubert & Anderson, 1985), as can be seen in Figure 5d, in which higher degrees are enhanced and dominate as compared to the basally heated case (note the low amplitude in power for $l = 2$). While the homogeneous T_s system moves to smaller aspect ratio convection, an inspection of the power spectra plot (Figure 5h) of the latitudinally variable T_s system shows that the $l = 2$ power still dominates, and that the muted expression of this degree-2 pattern at the surface is the result of enhanced power in higher degrees. The ratio of total $l = 2$ power to the total power of the convective system is similar to the $\Delta\eta = 10^2$ cases, with less than 1% for the homogeneous case and 12% for the latitudinally variable T_s case. An implication from Schubert and Anderson (1985) is that the total convective power should decrease, and the total power for mixed heating cases ($Q = 49$) decreases by 41% (homogeneous) and 18% (latitudinally variable) as compared to the basally heated cases. Compared to the basal heating case, bulk system (and consequently surface) velocities decrease by ~19%, consistent with the findings of O'Farrell and Lowman (2010) for principally Cartesian geometries as well as Weller et al. (2016) for spherical shell geometries with a core fraction of 0.54 (see Weller et al., 2016; Weller & Lenardic, 2016). Consequently,

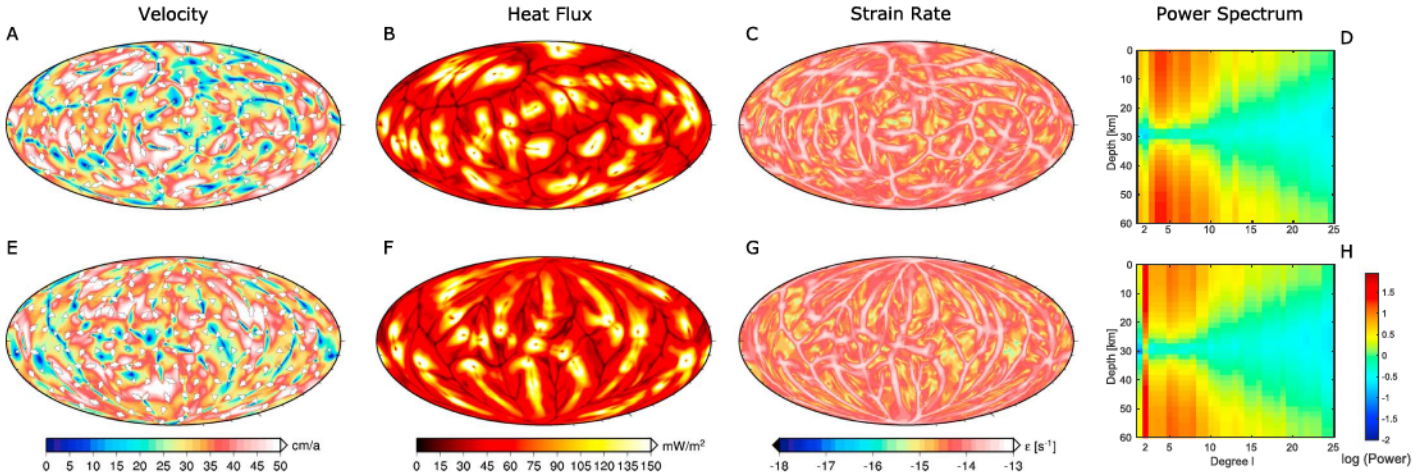

Figure 7. Moderate *Ra* isoviscous basally heated results for homogeneous (top row) and latitudinally variable (bottom row) surface temperatures. Plots show surface velocity field (a, e), heat flux (b, f), strain rate (c, g), and the log of the poloidal power spectra (d, h). The basal *Ra* is fixed at $7{\cdot}10^5$, and both the average surface temperatures are the same in each model. Arrows denote surface flow direction. Quantities are dimensionalized following equation (6) with property values denoted in the Figure 1 caption.

strain rates similarly decrease (Figure 5c and 5g). Mobilities are ~1.11 and ~1.08 for the homogeneous and latitudinally variable T_s cases, respectively, a difference of less than 3% that similarly falls near the natural variability of the systems (~ 1%). These values are marginally smaller than the ~1.2 value obtained in the comparable basal heating cases. Average surface velocity similarly follows as being less than ~ 1,700 (~ 20 cm/a) due to decreases in both mobility and bulk average velocities. The average and maximum surface stress is largely unchanged from the basally heated case with τ_{mean} ~ 1 Pa and τ_{max} ~ 19 Pa for both the homogeneous and latitudinally variable T_s conditions.

Next, we consider an example temperature-dependent viscosity system, with a viscosity contrast of 10^3, and the *Ra* and internal heating rates identical to the previous case. In contrast to the isoviscous cases, the net effect of increasing *Q* on the system behavior is one of stabilization and amplification. In the homogeneous T_s case, there is an upwelling zone in the Northern Hemisphere and a ring-like downwelling feature surrounding an upwelling zone in the Southern Hemisphere (Figure 6a). Both upwelling zones are nearly antipodal. Heat flux and strain rate are maximal in the Northern Hemisphere and minimal in the Southern

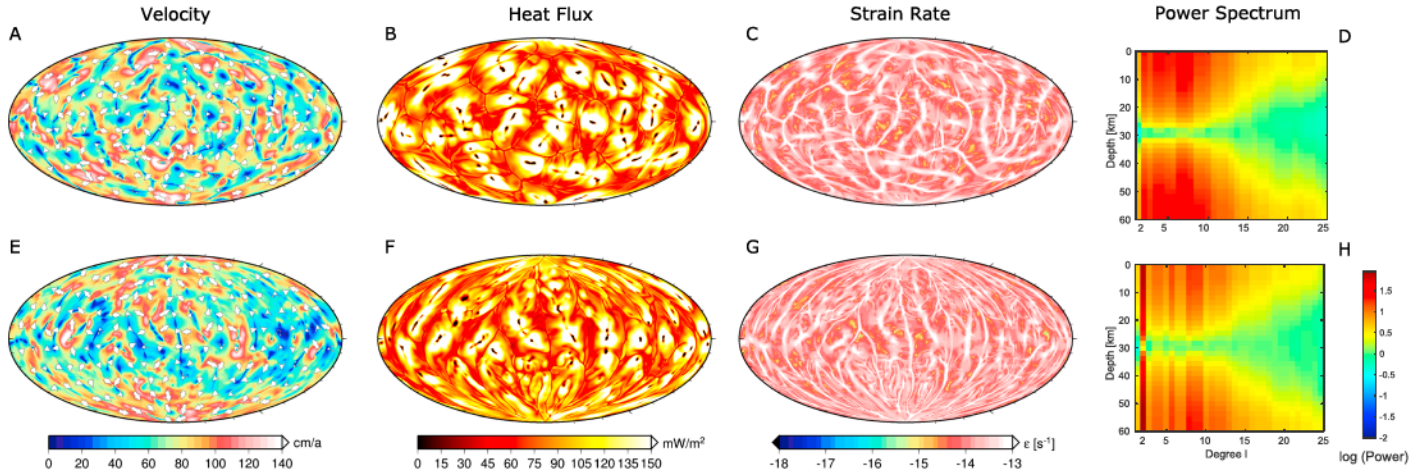

Figure 8. High *Ra* isoviscous basally heated results for homogeneous (top row) and latitudinally variable (bottom row) surface temperatures. Plots show surface velocity field (a, e), heat flux (b, f), strain rate (c, g), and the log of the poloidal power spectra (d, h). The basal *Ra* is fixed at $3{\cdot}10^6$, and the average surface temperatures for each model are the same. Arrows denote surface flow direction. Quantities are dimensionalized following equation (6) with property values denoted in the Figure 1 caption. Note for clarity that the scale range differs from the isoviscous cases in Figure 1.

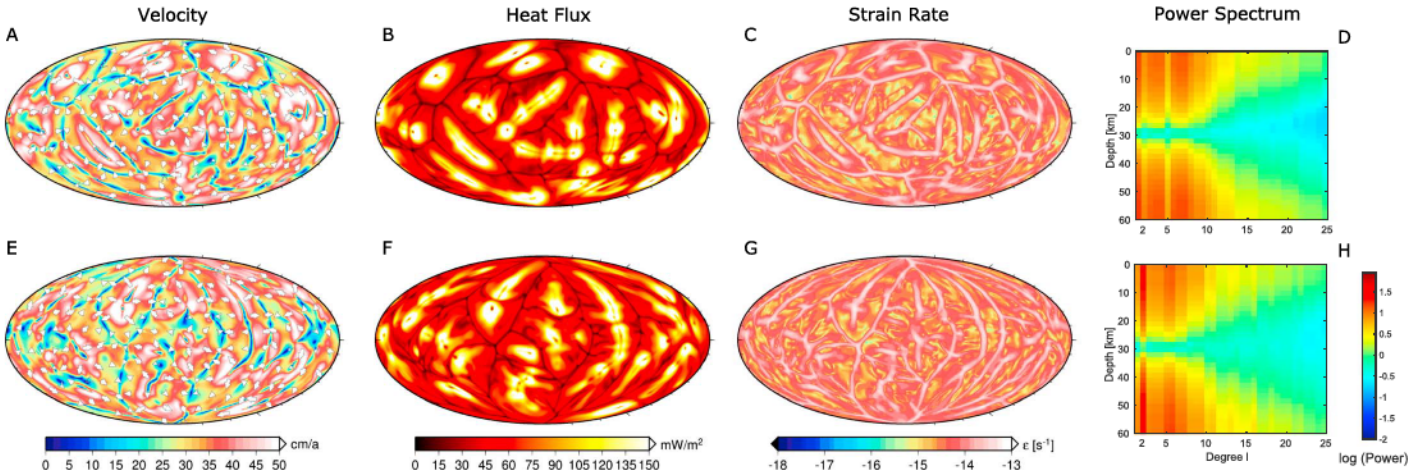

Figure 9. Basal heating isoviscous results with half variation in surface temperatures (T_s ~ 8% of the basal temperature) for homogeneous (top row) and latitudinally variable (bottom row) surface temperatures. Plots show surface velocity field (a, e), heat flux (b, f), and strain rate (c, g), and the log of the poloidal power spectra (d, h). The basal *Ra* is fixed at $7{\cdot}10^5$, and the average surface temperatures for each model are the same. Arrows denote surface flow direction. Quantities are dimensionalized following equation (6) with property values denoted in the Figure 1 caption.

Hemisphere (besides the small upwelling zone contained within the downwelling curtain; Figures 6c and 6d). In contrast, the latitudinal T_s case has an enhanced upwelling plume anchored on the equator (Figure 6f). Surface velocities are oriented radially from the plume center. This configuration leads to high heat flux within about 20% of the domain and minimal heat flux antipodal to the equatorial upwelling (Figure 6h). Strain rates are maximal in both polar regions (Figure 6i). Surface (and bulk internal) velocities increase from the basally heated case (an increase of a factor of ~1.8 bulk internal and ~2.8 surface velocities). Likely, this is due to both the long wavelength convection cells that become established and the increasing bulk system velocities from increased internal temperatures reducing the viscous resistance to flow. An inspection of the power spectra for both cases reinforces this large-scale structure (Figures 6e and 6k). Degree-1 one convection strongly dominates both systems, with a very small $l = 2$ signal in the lower and upper portions of the domain. The ratio of total $l = 2$ power to the total power of the convective system is ~6% for both the homogeneous and latitudinally variable T_s cases. The total power for both mixed heating cases ($\Delta\eta = 10^3$, $Q = 49$) increases by between 45% and 49% as compared to the basally heated cases at the same parameter value, opposite the results of the isoviscous cases. This signifies that while the variable

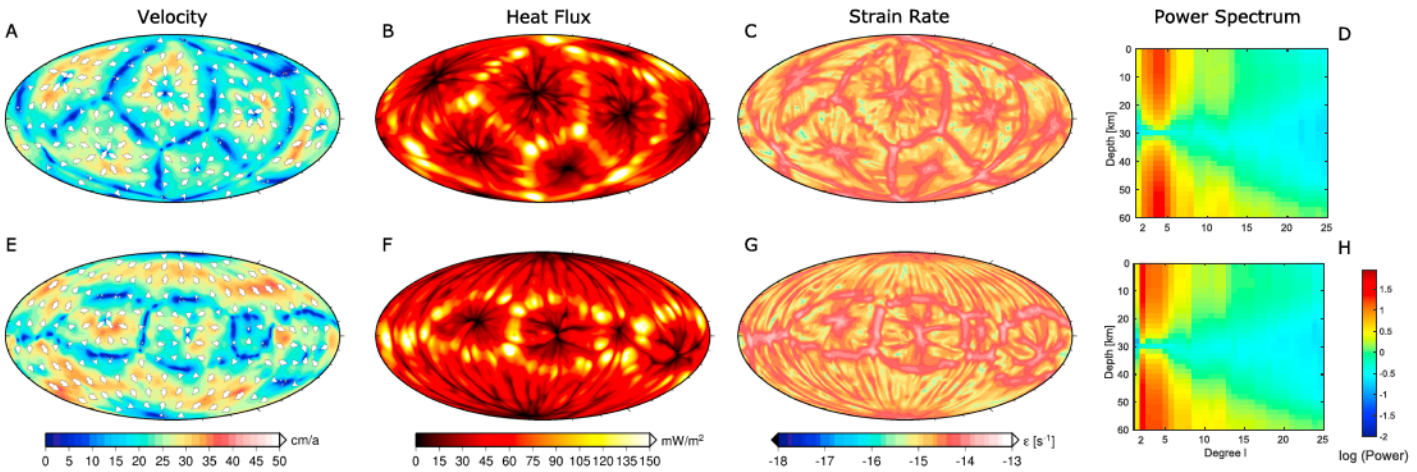

Figure 10. High *Ra* with temperature-dependent viscosity for homogeneous (top row) and latitudinally variable (bottom row) surface temperatures. Plots show surface velocity field (a, e), heat flux (b, f), strain rate (c, g), and the log of the poloidal power spectra (d, h). The basal *Ra* is fixed at $3{\cdot}10^6$, $\Delta\eta = 10^2$, and the average surface temperatures for each model are the same. Arrows denote surface flow direction. Quantities are dimensionalized following equation (6) with property values denoted in the Figure 1 caption. Note for clarity that the scale range differs from the isoviscous cases in Figure 1.

insolation is changing the flow characteristics of the shell (orientation of surface velocities Figures 6a and 6f), it is not the dominant effect. Instead, the internal stabilizing effects of both high internal heating and intermediate viscosity contrast ($\Delta\eta = 10^3$) control the aspect ratio of the convective system. In these cases, the net effect of variable insolation is to reorient the upwelling zone to the equator. Mobilities are ~1.10 and ~1.16 for the homogeneous and latitudinally variable T_s cases, respectively, which is similar to the isoviscous cases at ~1.1, presumably due to the reduction in bulk viscosity from higher internal temperatures and the long wavelength of convection. Average surface velocities are 469 (5.35 cm/a) and 524 (5.98 cm/a). Average surface stresses increase to τ_{mean} ~ 0.06 kPa and ~ 0.3 kPa and stress maxima increase substantially to τ_{max} ~ 2.24 and ~ 13.53 kPa for the homogeneous and latitudinally variable T_s cases, respectively.

We now consider the robustness of both increasing basal *Ra* numbers with variable surface temperatures and decreasing the total temperature contrast across the surface. First, we focus on isoviscous systems with no internal heating, basal *Ra* of $7{\cdot}10^5$ (Figure 7) and $3{\cdot}10^6$ (Figure 8), and the same fixed average surface temperature as before. In both cases, similar to the lower *Ra* system, the latitudinally variable T_s leads to a poleward flow of material and longitudinally elongated convection cells, despite the higher convective vigor. Similarly, reducing the average surface temperature variation amplitude has the net effect of increasing the system's effective *Ra*. Qualitatively, a reduction in the average T_s variation by 50% (to ~8% the base of the ice shell), should increase the effective *Ra* by a factor of 2. Indeed, an inspection of Figure 9, which has otherwise identical input parameters of those of Figure 7, indicates a qualitative agreement with the nominal $Ra = 7{\cdot}10^5$ models. The orientations of the convective cells are still affected and organized by the variation in surface temperature despite a total reduced magnitude. The ratio of the $l = 2$ to total convective power decreases to negligible levels (< 1%) for the homogenous T_s case and decreases slightly to 16% for the variable T_s case (Figure 7), as compared to the nominal isoviscous cases ($Ra = 3{\cdot}10^5$). In Figure 9, as compared to Figure 7, the 8% T_s variation cases show that the power is distributed more broadly, though $l = 2$ still dominates the power spectrum of the variable T_s case. The ratio of $l = 2$ power to the total power of the convective system is 1% for the homogeneous T_s case and drops to 11% for the latitudinally variable T_s case.

The net effect of increasing the *Ra* under constant surface temperatures is generally to move the system to higher degree convection (Figures 7d and 7h, 8d and 8h, and 9a and 9h). While there is an increase in power at higher degrees, the variable insolation cases still indicate a dominant $l = 2$ signal. Interestingly, Figure 8h shows very little power away from $l = 2$, and while the ratio of $l = 2$ power to the total power of the convective system is less than a percent for the homogeneous T_s case, it increases (relative to the lower *Ra* cases) to 21% for the latitudinally variable T_s case ($Ra = 3{\cdot}10^6$).

Increasing the viscosity contrast to 10^2 shows a very similar response, the ratio of $l = 2$ power to the total power of the convective system is 6% for homogeneous T_s case, and it remains elevated at 18% for the latitudinally variable T_s case ($Ra = 3{\cdot}10^6$; $\Delta\eta = 10^2$). Intermediate viscosity contrasts ($\Delta\eta = 10^2$) with a $Ra = 3{\cdot}10^6$ (Figure 10) and additional higher viscosity contrasts cases ($\Delta\eta > 10^3$) qualitatively show little difference in the surface flow field, heat flux, and strain rates from the reference *Ra* cases in Figure 3. Once stagnant, increasing the viscosity contrast to $3{\cdot}10^4$ indicates similar behavior and is not qualitatively different from other high viscosity reference *Ra* cases (Figures 4c and 10). For this case, the $l = 2$ to total power ratio is 1% for the homogeneous T_s case (nearly identical to the case of Figure 4c) and increases by nearly a factor of 2 to 9% for the latitudinally variable T_s case (as compared to Figure 4c). These results strongly indicate that a significant increase in *Ra* for latitudinally variable T_s cases acts to amplify the power of $l = 2$, and the hemispheric flow pattern compared to lower *Ra*, while the homogeneous T_s case favors higher degree convection, suggesting that the upper bounds on the *Ra* calculated for each satellite (Table 1) may act to reinforce degree-2 style convection from variable solar insolation.

Mobility for all surface temperature cases and *Ra*'s are unaffected from previous isoviscous experiments, with values that are within a few percent of 1.2. For the isoviscous systems, average surface velocities increase from the initial reference case ($Ra = 3{\cdot}10^5$) to ~ 2,700 (~ 31 cm/a) for $Ra = 7{\cdot}10^5$ and ~ 6,000 (~ 68 cm/a) for $Ra = 3{\cdot}10^6$, for both T_s cases. Maximum surface stresses increase from the reference cases to τ_{max} ~ 41 Pa (τ_{mean} ~ 2 Pa) for $Ra = 7{\cdot}10^5$ and ~ 120 Pa for $Ra = 3{\cdot}10^6$ (τ_{mean} ~ 6 Pa), for both T_s cases, suggesting greater localization of stress as the *Ra* increases. With moderate temperature-dependent

viscosity (10^2) for the $Ra = 3{\cdot}10^6$ cases, velocities increase from the reference Ra case to 1,758 (20 cm/a) and 1,954 (22 cm/a), for the homogeneous and latitudinally variable T_s cases, respectively. Increasing the viscosity contrast to $3{\cdot}10^4$ ($Ra = 3{\cdot}10^6$) results in velocity increases (from the $Ra = 3{\cdot}10^5$ and $\Delta\eta = 10^4$ case) to 16 (~0.2 cm/a) and 47 (~0.6 cm/a), for the homogeneous and latitudinally variable T_s cases, respectively. Stresses similarly increase. With intermediate viscosity contrasts (10^2), the stresses for the homogeneous case reach $\tau_{max} = 1.0$ and $\tau_{mean} = 0.05$ kPa and for the latitudinally variable case, $\tau_{max} = 3.3$ and $\tau_{mean} = 0.08$ kPa. For a viscosity contrast of $3{\cdot}10^4$, the homogeneous case is $\tau_{max} = 6.8$ and $\tau_{mean} = 0.2$ kPa, and the latitudinally variable case is $\tau_{max} = 40$ and $\tau_{mean} = 0.6$ kPa. The preceding simulations indicate that the effects of a latitudinal variation in surface temperature are robust over the tested range of physically plausible parameters and convective vigors that would be expected for the icy satellites.

4. Discussion and Implications

It has previously been shown that variability in solar insolation may be a significant control on Mercury's geoid and topography through the generation of hotlines due to its eccentric orbit and phase locking (Tosi et al., 2015), and may also have a significant effect on flow patterns and volcanism on tidally locked exoplanets (van Summeren et al., 2011). Our work expands on these studies by examining the underlying physics of latitudinally variable insolation with applications to thin shell convection appropriate for the icy satellites. Our results illustrate that higher surface temperatures along the equator thin the boundary layer locally, enhancing upwellings and heat flow, while colder surface temperatures at the poles lead to thickened boundary layers and enhanced downwelling zones. For the isoviscous and low viscosity contrast regimes, a hemispheric flow pattern develops that looks akin to an atmospheric Hadley cell (for a different fluid dynamical regime, of course, but similar driving forces). In all cases, surface velocity field orientations generally transport material poleward from the equator, though increasing viscosity contrasts generally dampen this effect it is still present. In the low Ra number regimes ($3{\cdot}10^5$), homogeneous T_s cases typically exhibit strong asymmetry in upwelling and downwelling sites (e.g., strong downwelling in the northern pole, Figure 4a, panel B).

For the isoviscous results, the $l = 2$, $m = 0$ component of the poloidal power spectrum can be explored as a function of changing Ra and T_s amplitude. The latitudinally variable T_s cases indicate a general trend of increased $l = 2$ with increasing Ra and decreased $l = 2$ strength with decreasing T_s amplitude (see Table 2 for additional values not shown in figures). The power of $l = 2$ increases from the homogenous surface temperature (average $T_s \approx 0.105$) cases by ~ 390% with $Ra = 3{\cdot}10^5$ (Figure 2), ~ 6,600% for $Ra = 7{\cdot}10^5$ (Figure 7), ~ 11,400% with $Ra = 3{\cdot}10^6$ (Figure 8), and ~ 660% for $Ra = 7{\cdot}10^5$ with an average $T_s \approx 0.05$ (Figure 9). The homogenous T_s cases indicate decreasing importance of $l = 2$ power with increasing Ra, which is expected as the higher Ra systems favor higher degree convection. As the T_s amplitude variation decreases, the variation in $l = 2$ power decreases, as expected. The principle implication for isoviscous systems with a larger Ra than we explicitly consider here is that the power differential between the homogenous and latitudinally variable T_s conditions should become much greater as the $l = 2$ component becomes preferentially enhanced with increasing vigor of convection under the condition of the latitudinally variable surface temperatures driving force.

Considering next the added complexity of temperature-dependent viscosity systems, the power of $l = 2$ in the system becomes dampened somewhat from the isoviscous conditions, though it remains an important effect. With the exception of the degree-1 style intermediate viscosity cases ($\Delta\eta = 10^3$), all variable T_s conditions show appreciably more power, often at least an order of magnitude, in $l = 2$ power as compared to their respective homogenous T_s cases. The power of $l = 2$ increases from the homogenous surface temperature cases by ~ 650% for $Ra = 3{\cdot}10^5$ and $\Delta\eta = 10^2$ (Figure 4a), ~ 9% for $Ra = 3{\cdot}10^5$ and $\Delta\eta = 10^3$ (Figure 4b), and ~ 890% for $Ra = 3{\cdot}10^4$ and $\Delta\eta = 10^4$ (Figure 4c). Increasing the Ra ($3{\cdot}10^6$) results in an increase of ~ 180% and ~340% for $\Delta\eta = 10^2$ and $\Delta\eta = 3{\cdot}10^4$, respectively (Figure 10 and Table 2). Similar to the isoviscous systems, increasing the vigor of convection for a given viscosity contrast increases the effective power in $l = 2$.

The cases with increasing internal heating rates (Table 2) suggest that heat production generally acts to dampen the $l = 2$ power, though not uniformly. In the variable T_s cases, the effect is minor as compared to the homogenous T_s cases. This suggests variable T_s counteracts the decrease in the wavelength of convection that occurs with high heating rates, though not completely as the absolute value of $l = 2$ in the system

drops (but it still remains significant). The power of $l = 2$ increases from the homogenous surface temperature case by ~ 2,700% with $Ra = 3{\cdot}10^5$, $Q = 49$ (Figure 5). In contrast, adding temperature-dependent viscosity with internal heating tends drives the system to a different condition, that of strengthening of $l = 2$ with increasing Q (Table 2). This may be due, in part, to system velocities increasing slightly with increasing Q, as opposed to the decrease noted with isoviscous systems. In aggregate, these results indicate that higher Ra and large amounts of internal heat generation with temperature-dependent viscosities may act to reinforce the expression of a Hadley type convection pattern within ice shells.

While the effects of a pole to equator variation in surface temperature in general are more pronounced for isoviscous and low viscosity contrast systems, the effects are shown clearly to still be present in the stagnant lid cases tested. Here the viscosity in the equatorial region is reduced, allowing for local movement of surface material toward the poles (movement is limited to the upper layer of the stagnant lid and as such does not interact with the interior directly). However, the higher viscosity at the minimum surface temperature precludes further movement, and material converges toward the midlatitudes, predicting regions of large strain. Internally, the thickened polar and thinned equatorial boundary layers tend to drive a flow pattern under the stagnant lid that mimics the Hadley type cell configuration of the lower viscosity contrast regimes. An important aspect of icy satellite convection that we currently neglect is the spatial variation in tidal heating. While it is currently unclear how spatial distributions in tidal heating would explicitly effect these results, a speculation can be made through a comparison of the basal and mixed heated cases. With the exception of the intermediate viscosity case ($\Delta\eta = 10^3$), the $l = 2$ component remains dominant despite increasing internal heating, from basally heated to maximal internal heating levels (Figures 2 and 4–9). Stagnant lid results with internal heating (not shown) do not display a significant deviation from a general poleward degree-2 style flow path. This suggests that the $l = 2$ power may remain significant in the case of spatially varying tidal heating. The addition of spatially varying tidal heating may not result in a significant difference in convective metrics at the global scale. Tidal heating that occurs preferentially at the poles may be expected to become mixed into the interior of the convective system, becoming more equilibrated with time. The effects of spatially varying tidal heating may be more significant for local or regional scales, particularly in regards to regional boundary layer effects. However, adding spatial variations in tidal effects adds to the complexity of the system and remains to be tested.

Another important aspect that we do not explicitly address in this work are the effects of long wavelength changes of the basal ice shell geometry due to variable insolation. An implication may be for a thinning of the ice shell along the equator and a thickening along the poles. Given the dependence of the Ra on layer depth (equation (4)), the prediction would be for a reduced effective Ra at the equator and enhanced poleward. The local effective Ra (equatorial and polar) in our system reflects this condition simply as a function of variable solar insolation, the equatorial effective Ra is reduced, and the polar effect enhanced. Addition of long wavelength variations in the base of the ice shell would likely greatly enhance our results. However, there may be negative feedback processes that could inhibit these effects. As an example, the ice shell may thin sufficiently that convection ceases. In this case, the poleward transport of material and the Hadley type cell structure would cease to operate. However, the expression of this cell could still be visible in the fabric of the ice shell. A caveat is that for any of the flow patterns shown in this work, there may be enough of a mass redistribution that a reorientation of the ice shell could perhaps be triggered (True Polar Wander; e.g., Nimmo & Pappalardo, 2006; Schenk, 2017), changing the relative driving forces and perhaps reorienting or shutting down the Hadley type cells.

A key effect of variable solar insolation is to generate global flow patterns that contribute in systematic ways to other stresses that are also acting to deform the ice shell. Therefore, it is of interest to assess the magnitudes of the convective stresses that are generated. Peak stresses in our models range from ~ 16 Pa (isoviscous) to ~ 40 kPa ($Ra = 3{\cdot}10^6$, $\Delta\eta = 3{\cdot}10^4$; variable insolation). Considering Europa, these stresses may be directly comparable to Europa's diurnal tides (~50 kPa; Wahr et al., 2009). In the case of Enceladus, these stresses are approximately within a factor of 2 of predicted upper bound tidal stresses operating on the tiger stripes (~100 kPa; Nimmo et al., 2007). Our model stresses are well below the several megapascal stresses predicted for ocean pressurization associated with ice shell thickening as the ocean slowly freezes and potential reorientation of the ice shell/nonsynchronous rotation (e.g., Manga & Wang, 2007; Matsuyama & Nimmo, 2008). Although processes generating stresses on the order of megapascal might be expected to dominate deformation of these bodies, this may not be the full story. Geologic evidence on Enceladus

(e.g., Crow-Willard & Pappalardo, 2015; Spencer et al., 2009), for example, suggest that ice shells may be pervasively fractured. Further, the ice may be damaged from impact events, have preexistent natural flaws in the ice structure (Hammond et al., 2018), or experience cyclic grounding and floating ice shell states (Johnston & Montési, 2017), all of which, in addition to fracturing, would reduce the strength and capacity of the ice shell to support various stresses (Bassis & Jacobs, 2013). In these scenarios, relatively low amplitude, variable insolation can set up a consistent, global, stress state in which convective stresses may serve to control deformation after the ice shell is fractured or damaged. The inference then is that a variation in solar insolation may drive significant deformation, both in isolation and in concert with other processes. For this work, we use a nominal variable surface temperature value of ~16% of the melting temperature of water ice. For the Galilean satellites, this value is likely to be appropriate (Table 1, e.g., Nadeau & McGehee, 2017; Ojakangas & Stevenson, 1989). However, for the Saturnian or Uranian satellites, a lower surface temperature variation of ~8% is more applicable. Our results illustrate that either variation results in similar flow patterns. While these values may be representative for the current state of the solar system, they almost certainly were not in the past, and nor will they be in the future. One process that could affect the surface temperature variation is that of the albedo. The albedo may be expected to change through time for these bodies, as it may be affected by tectonism and cryovolcanism as well as degradation and alteration of the surface from impact processes, high energy particle interactions, and space weathering (e.g., Schenk et al., 2011). Another important process to consider is that of solar luminosity variation. It is well known that as stars age, their solar luminosity is expected to increase (e.g., Feulner, 2012; Sagan & Mullen, 1972). Consequently, early in the solar system, the effects of latitudinally variable surface temperatures on the icy bodies would be muted as solar insolation would have been reduced by ~30% at ~4.4 Ga (e.g., Bahcall et al., 2001; Gough, 1981). However, as the star ages and insolation increases, the driving force that the variation in solar insolation induces is expected to become increasingly important. The surface temperature variation representative of the satellites considered for the Saturnian system in the present may be representative of the surface temperature variation (in relation to the melting temperature of ice) in the Galilean system a few gigayears ago, and the Galilean system may be a prediction for the surface temperature distribution a few gigayears in the future for the Saturnian system (see supporting information). Therefore, each satellite system can be considered a snapshot of different times and locations in the Solar System.

Latitudinally variable insolation has interesting implications for icy satellites. A key characteristic for these systems is a thickened boundary layer at the poles and a thinned thermal boundary layer along the equator. This has important consequences for quantities such as the elastic thickness of the ice shell. In the context of temperatures, the elastic thickness depends on the surface temperature and the thermal profile of the ice shell. Flexural effects, while important (e.g., McNutt, 1984), are neglected in this simple thought experiment. The thickened thermal boundary layer results in a deepening of the elastic layer depth. In contrast, the thinned thermal boundary layer along the equator results in a shallowing of the elastic layer base. In general, it can be inferred that the effect of latitudinally variable insolation is to mechanically strengthen the ice shell (able to accommodate higher stresses and able to support larger loads before failure) toward the pole, and weaken it toward the equator, neglecting spatial distributions in tidal heating. This suggests that the hemispheric variation in surface temperatures can lead to potential local enhancement of stress and failure (as shown by the stress results). Further, due to changes in the thermal boundary layer thicknesses, heat flux is enhanced toward the equator and suppressed near the poles (e.g., Figure 3b, panels C, G, K). This may be important for processes such as viscous relaxation (e.g., Bland et al., 2012). Both the homogeneous and latitudinally variable cases exhibit a strong heterogeneity of both thermal boundary layer thicknesses and heat flux linked to upwelling and downwelling zones (the locations themselves differ for each case). The key implication is that in either of these cases, viscous relaxation should not be expected to be uniform across the surface, and indeed significant variations linked to internal convection should exist. As such, it may not be always clear if the relaxation at the surface is reflective of the global mean or some local minima/maxima.

A second interesting consequence of variable insolation relates to the global flow field. For low viscosity contrast regimes and high viscosity stagnant lids, hemispheric-scale convection cells are established. This structure is largely disrupted in favor of a spherical harmonic degree-one style (upwelling- and downwelling-dominated hemispheres) convective systems for intermediate viscosity contrasts. For

viscosity contrasts $\Delta\eta \lesssim 10^2$, material is principally transported toward the poles with a return flow to the equator at the base of the ice shell. For stagnant lids, this flow is isolated under the lid. Velocities in the center of a convective cell are negligible (e.g., Turcotte & Schubert, 2005); this region is often small for standard Rayleigh-Bénard style convective cells and becomes elongated from the equator to the pole in our experiments. This elongation indicates that a planar layer of contrasting velocities (low velocity interior to high velocity exterior) exhibiting high shear would exist through large portions of the middle of the ice shell (Figures 2 and 4; similar to shear in the Earth's mantle, e.g., Becker, 2017). This region would likely have a strong preferred crystallographic orientation and associated anisotropy that may be detectable with radar and seismic acquisitions of active ice shells such as expected for Europa (e.g., Barr & Stillman, 2011; Panning et al., 2018; Rudolph & Manga, 2012; Vance et al., 2018).

The global flow field further results in strain rates that are enhanced along the equator (for all viscosity contrasts), the midlatitudes (stagnant lid cases), and has a preferred nearly longitudinal orientation (Figures 1, 3b, 5, 7, 9) that becomes arcuate and circular (Figure 3b, panels D and H) as the viscosity contrast increases (up to the limit of the stagnant lid). Deformation would likely then be concentrated along portions of the equator, perhaps discontinuously, or radiating arcuate patterns, the surface expression of which may be strongly asymmetric (Figure 3b, panel H). Interestingly, the stagnant lid case exhibits enhanced surface velocities along the equator in a patch work structure. The orientations are poleward but quickly are dampened by the higher viscosities. This suggests the potential for quasi-circular regions of extension in the center (orientated near the equator) and compression along the edges (orientated in the midlatitudes), the expression of which may be analogous to a simple rift basin (e.g., Walker et al., 2012).

A third interesting aspect of the internal metrics in thin shell geometries is their divergence from thick shell geometries and Cartesian cases (cf. Guerrero et al., 2018). Probably, the most significant effect of increasing f is on the internal temperature (e.g., Jarvis et al., 1995). As the core fraction increases (ice shell domain shrinks), internal temperatures increase and approach the basal temperature for high core fractions (e.g., King et al., 2010). This occurs due to heat flux conservation of higher-energy density at the base of the ice shell due to the large core (basal heat flux increases with increasing core surface area) as f approaches unity, that is, the inner and outer surface areas of the shells become more equal. The mean temperature effect has implications for thin shell satellites such as Europa (Table 1): the internal temperatures would be predicted to be near the melting temperature of water ice throughout the convecting ice shell. Therefore, on Europa, this effect would likely predict much more activity, such as cryovolcanism and tectonism due to thinner boundary layers and consequently weaker ice from the high internal temperatures, than Enceladus (outside of the thin South Polar Terrain). Although this argument assumes canonical basal heating relationships that may not fully hold for these systems as the boundary layers are likely to strongly interact (e.g., Weller et al., 2016), first-order observations of deformation on the surfaces of Enceladus and Europa are suggestive. For example, in contrast to inferred paleo-equatorial basins on Enceladus that are likely associated with stagnant lid convection (Besserer et al., 2013; Schenk & McKinnon, 2009; Tajeddine et al., 2017), the equatorial region of Europa is characterized by areas of disrupted ice known as chaos terrains (e.g., Collins & Nimmo, 2009). Since these features may be associated with diapirism and the presence of liquid water in the subsurface (e.g., Pappalardo et al., 1998; Schmidt et al., 2011; Sotin et al., 2002), the combination of a geometrically thin shell, internal temperatures near the melting point of ice, and latitudinally variable surface temperatures may contribute to this distribution. In this context, holding all else equal, the same process of a latitudinal variation in insolation can be predicted to have different expressions at the surface for both satellites.

The previous discussion focuses on Europa and Enceladus due to their current level of activities, which make them prime candidates to identify processes associated with latitudinally variable insolation. While a complete survey of mid to large sized icy bodies is impractical (and beyond the scope of this work), it is of interest to also consider a less active satellite, notably Miranda, within the context of convection with latitudinally variable insolation. Miranda is inferred to be dominated by regions of old cratered terrain overprinted by three large *coronae* structures that fall along an arc across the surface (Smith et al., 1986). Recently, it has been suggested that the so-called coronae and associated resurfacing of the satellite are the results of sluggish lid or low viscosity contrast convection (e.g., $\Delta\eta = 10^3$, Hammond & Barr, 2014a). While the work of Hammond and Barr (2014a) considers more vigorous convection, tidal heating

distributions (e.g., Beuthe, 2013; Tobie et al., 2005), a constant T_s of 60 K, and small core fractions, our models with latitudinally variable insolation (e.g., Figure 3b, panel G) show similar results at lower *Ra* and higher core fractions. This suggests that there may be an interesting interplay between latitudinally variable insolation, tidal heating, and vigor of convection that has yet to be explored.

Our work provides a foundation for understanding complex convective systems that more closely emulate icy satellite evolution and development. In our approach, we currently consider uniform internal heating for our mixed heating models, which is likely a poor approximation for tidal heating effects. Additionally, we do not yet consider the effects of plastic yielding or weakening to emulate large-scale plastic deformation of the ice shell. Yielding formulations allow for mobility of the surface and interaction with the interior despite the formation of high viscosity *lids*. The implication is that the system will operate in an effective intermediary viscosity regime, that is, some combination of viscosity contrast results explored here. Further, we do not consider melting or compositional variations within the ice shell in this work. All processes are likely to be important for the expression of deformation of the ice shell, and remain to be explored.

5. Conclusions

Numerical experiments of spherical, thin-shell convection show what effects a latitudinal variation in solar insolation may have on convective dynamics. A global flow pattern of upwelling equatorial regions and downwelling polar regions, linked to higher and lower surface temperatures, respectively, is preferred. As expected due to the gradient in surface temperatures, boundary layer thicknesses vary from equatorial lows and polar highs, and polar oriented flow fields are established.

For low viscosity contrast regimes, this results in a Hadley cell type configuration, with two hemispheric-scale convective cells emerging. Heat flow in these systems is enhanced along the equator and reduced along the poles. For intermediate viscosity contrast systems, larger-scale plume structures emerge, focused on the equator. Heat flow in this case is focused in the hemispheric-scale plume and suppressed in the antipodal hemisphere. For the highest viscosity contrast systems, the thick stagnant lid separates a hemispheric-scale internal convective cell from a geographically limited poleward orientated velocity field at the surface. Heat flow in this case has similarities to both of the previous cases where maxima are focused in discrete upwelling plumes that are more common along the equator and less common near the poles. Outside of these small plumes, heat flux is negligible, illustrating that heat flow is highly heterogeneous within the stagnant lid system.

The Hadley cell style poleward transport of material is robust under a variety of conditions: mixed heating with a high degree of internal heat generation, increased vigor of convection, and a range of surface temperature variations. In all cases, the structures are subdued compared to the initial basal heating cases, but the variation in insolation remains a significant control on the expression of mantle convection. Together, these results suggest that a latitudinal variation in surface temperature is an important effect for convection within the thin ice shells of the outer satellites; offers general testable predictions of lower heat flow and more compressional deformation near the poles and midlatitudes, more extensional equatorial regions with higher heat flow; may contribute to the location and expression of tectonic features; and likely becomes increasingly important as the Sun ages.

Acknowledgments
The authors would like to thank the Editor Sabine Stanley and two anonymous referees for their constructive reviews that helped improve the clarity of the manuscript. Funding for this work was provided by NASA grant 80NSSC18K0279. Resources supporting this work were provided by both the Texas Advanced Computing Center (TACC) at The University of Texas at Austin (URL: https://www.tacc.utexas.edu) and the NASA High-End Computing (HEC) Program through the NASA Advanced Supercomputing (NAS) Division at Ames Research Center. Pursuant to AGU guidelines, data for this paper are provided within the publication pages, in particular the tables and figures, and further made on Zenodo (Weller et al., 2019).

References

Bahcall, J. N., Pinsonneault, M. H., & Basu, S. (2001). Solar models: Current epoch and time dependences, neutrinos, and helioseismological properties. *The Astrophysical Journal*, *555*(2), 990–1012. https://doi.org/10.1086/321493

Barr, A. C. (2008). Mobile lid convection beneath Enceladus' south polar terrain. *Journal of Geophysical Research*, *113*, E07009. https://doi.org/10.1029/2008JE003114

Barr, A. C., & Hammond, N. P. (2015). A common origin for ridge - and - trough terrain on icy satellites by sluggish lid convection. *Physics of the Earth and Planetary Interiors*, *249*, 18–27. https://doi.org/10.1016/j.pepi.2015.09.009

Barr, A. C., & McKinnon, W. B. (2007). Convection in Enceladus' ice shell: Conditions for initiation. *Geophysical Research Letters*, *34*, L09202. https://doi.org/10.1029/2006GL028799

Barr, A. C., & Preuss, L. J. (2010). On the origin of south polar folds on Enceladus. *Icarus*, *208*, 499–503. https://doi.org/10.1016/j.icarus.2010.3.038

Barr, A. C., & Stillman, D. E. (2011). Strain history of ice shells of the Galilean satellites from radar detection of crystal orientation fabric. *Geophysical Research Letters*, *38*, L06203. https://doi.org/10.1029/2010GL046616

Bassis, J. N., & Jacobs, S. (2013). Diverse calving patterns linked to glacier geometry. *Nature Geoscience*, *6*(10), 833–836. https://doi.org/10.1038/ngeo1887

Becker, T. W. (2017). Superweak asthenosphere in light of upper-mantle seismic anisotropy. *Geochemistry, Geophysics, Geosystems*, *18*, 1986–2003. https://doi.org/10.1002/2017GC006886

Bender, K. C., Rice, J. W., Wilhelms, D. E., & Greeley, R. (1997). Geological map of Callisto. USGS Misc. Investigations Series, I-2581.

Bergstralh, J. T., Miner, E. D., & Matthews, M. S. (1991). *Uranus*. Tucson: University of Arizona Press.

Besserer, J., Nimmo, F., Roberts, J. H., & Pappalardo, R. T. (2013). Convection-driven compaction as a possible origin of Enceladus's long wavelength topography. *Journal of Geophysical Research: Planets*, *118*, 908–915. https://doi.org/10.1002/jgre.20079

Beuthe, M. (2013). Spatial patterns of tidal heating. *Icarus*, *223*(1), 308–329. https://doi.org/10.1016/j.icarus.2012.11.020

Beuthe, M., Rivoldini, A., & Trinh, A. (2016). Enceladus's and Dione's floating ice shells supported by minimum stress isostasy. *Geophysical Research Letters*, *43*, 10,088–10,096. https://doi.org/10.1002/2016GL070650

Bland, M. T., Singer, K. N., McKinnon, W. B., & Schenk, P. M. (2012). Enceladus' extreme heat flux as revealed by its relaxed craters. *Geophysical Research Letters*, *39*, L17204. https://doi.org/10.1029/2012GL052736

Bland, R. M., Yseboodt, M., & van Hoolst, T. (2016). The obliquity of Enceladus. *Icarus*, *268*, 12–31. https://doi.org/10.1016/j.icarus.2015.11.039

Cameron, M. E., Smith-Konter, B. R., Burkhard, L., Collins, G. C., Seifert, F., & Pappalardo, R. T. (2018). Morphological mapping of Ganymede: Investigating the role of strike-slip tectonics in the evolution of terrain. *Icarus*, *315*, 92–114. https://doi.org/10.1016/j.icarus.2018.06.024

Collins, G. C., McKinnon, W. B., Moore, J. M., Nimmo, F., Pappalardo, R. T., Prockter, L. M., & Schenk, P. M. (2010). In R. A. Schultz & T. R. Watters (Eds.), *Tectonics of the outer planet satellites, planetary tectonics* (pp. 264–350). Cambridge, UK: Cambridge University Press.

Collins, G. C., & Nimmo, F. N. (2009). *Chaotic terrain on Europa, in Europa after Galileo* (pp. 259–281). Tucson, AZ: University of Arizona Press.

Crow-Willard, E. N., & Pappalardo, R. T. (2015). Structural mapping of Enceladus and implications for formation of tectonized regions. *Journal of Geophysical Research: Planets*, *120*, 928–950. https://doi.org/10.1002/2015JE004818

Dahlen, F. A., & Tromp, J. (1998). *Theoretical global seismology*. Princeton, NJ: Princeton University Press.

Durham, W. B., & Stern, L. A. (2001). Rheological properties of water ice—Applications to satellites of the outer planets. *Annual Review of Earth and Planetary Sciences*, *29*(1), 295–330. https://doi.org/10.1146/annurev.earth.29.1.295

Feulner, G. (2012). The faint young Sun problem. *Reviews of Geophysics*, *50*, RG2006. https://doi.org/10.1029/2011RG000375

Glein, C. R., Baross, J. A., & Waite, J. H. (2015). The pH of Enceladus' ocean. *Geochimica et Cosmochimica Acta*, *162*, 202–219. https://doi.org/10.1016/j.gca.2015.04.017

Gough, D. O. (1981). Solar interior structure and luminosity variations. *Solar Physics*, *74*(1), 21–34. https://doi.org/10.1007/BF00151270

Greeley, R., Chyba, C. F., Head, J. W., McCord, T. B., McKinnon, W. B., Pappalardo, R. T., & Figueredo, P. H. (2004). Geology of Europa. In F. Bagenal, T. E. Dowling, & W. B. McKinnon (Eds.), *Jupiter: The planet, satellites, and magnetosphere* (pp. 363–396). Cambridge, UK: Cambridge University Press.

Greeley, R., Klemaszewski, J. E., & Wagner, R. (2000). Galileo Imaging Team, Galileo views of the geology of Callisto. *Planetary and Space Science*, *48*(9), 829–853. https://doi.org/10.1016/S0032-0633(00)00050-7

Grott, M., Sohl, F., & Hussmann, H. (2007). Degree-one convection and the origin of Enceladus' dichotomy. *Icarus*, *191*(1), 203–210. https://doi.org/10.1016/j.icarus.2007.05.001

Guerrero, J. M., Lowman, J. P., Deschamps, F., & Tackley, P. J. (2018). The influence of curvature on convection in a temperature-dependent viscosity fluid: Implications for the 2D and 3D modeling of moons. *Journal of Geophysical Research: Planets*, *123*, 1863–1880. https://doi.org/10.1029/2017je005497

Hammond, N. P., & Barr, A. C. (2014a). Global resurfacing of Uranus's moon Miranda by convection. *Geology*, *42*(11), 931–934.

Hammond, N. P., & Barr, A. C. (2014b). Formation of Ganymede's grooved terrain by convection-driven resurfacing. *Icarus*, *227*, 206–209. https://doi.org/10.1016/j.icarus.2013.08.024

Hammond, N. P., Barr, A. C., Cooper, R. F., Caswell, T. E., & Hirth, G. (2018). Experimental constraints on the fatigue of icy satellite lithospheres by tidal forces. *Journal of Geophysical Research: Planets*, *123*, 390–404. https://doi.org/10.1002/2017JE005464

Han, L., & Showman, A. (2010). Coupled convection and tidal dissipation in Europa's ice shell. *Icarus*, *207*(2), 834–844. https://doi.org/10.1016/j.icarus.2009.12.028

Han, L., Tobie, G., & Showman, A. P. (2012). The impact of a weak south pole on thermal convection in Enceladus' ice shell. *Icarus*, *218*(1), 320–330. https://doi.org/10.1016/j.icarus.2011.12.006

Helfenstein, P., & Parmentier, E. M. (1985). Patterns of fracture and tidal stresses due to nonsynchronous rotation: Implications for fracturing on Europa. *Icarus*, *61*(2), 175–184. https://doi.org/10.1016/0019-1035(85)90099-5

Howett, C. J. A., Spencer, J. R., Pearl, J., & Segura, M. (2011). High heat flow from Enceladus' south polar region measured using 10–600 cm^{-1} Cassini/CIRS data. *Journal of Geophysical Research*, *116*, E03003. https://doi.org/10.1029/2010JE003718

Jarvis, G. T., Glatzmaier, G. A., & Vangelov, V. I. (1995). Effects of curvature, aspect ratio and planform in two- and three-dimensional spherical models of mantle convection. *Geophysical and Astrophysical Fluid Dynamics*, *79*(1-4), 147–171. https://doi.org/10.1080/03091929508228995

Jia, X., Kivelson, M. G., Khurana, K. K., & Kurth, W. S. (2018). Evidence of a plume on Europa from Galileo magnetic and plasma wave signatures. *Nature Astronomy*, *2*, 459–464. https://doi.org/10.1038/s41550-018-0450-z

Johnston, S. A., & Montési, L. G. J. (2017). The impact of a pressurized regional sea or global ocean on stresses on Enceladus. *Journal of Geophysical Research: Planets*, *122*, 1258–1275. https://doi.org/10.1002/2016JE005217

Kattenhorn, S. A., & Prockter, L. M. (2014). Evidence for subduction in the ice shell of Europa. *Nature Geoscience*, *7*(201), 762–767. https://doi.org/10.1038/ngeo2245

King, E. M., Soderlund, K. M., Christensen, U. R., Wicht, J., & Aurnou, J. M. (2010). Convective heat transfer in planetary dynamo models. *Geochemistry, Geophysics, Geosystems*, *11*, Q06016. https://doi.org/10.1029/2010GC003053

Kirchoff, M. R., & Schenk, P. (2009). Crater modification and geologic activity in Enceladus' heavily cratered plains: Evidence from the impact crater distribution. *Icarus*, *202*(2), 656–668. https://doi.org/10.1016/j.icarus.2009.03.034

Kirk, R. L., & Stevenson, D. J. (1987). Thermal evolution of a differentiated Ganymede and implications for surface features. *Icarus*, *69*(1), 91–134. https://doi.org/10.1016/0019-1035(87)90009-1

Manga, M., & Wang, C.-Y. (2007). Pressurized oceans and the eruption of liquid water on Europa and Enceladus. *Geophysical Research Letters*, *34*, L07202. https://doi.org/10.1029/2007GL029297

Matsuyama, I., & Nimmo, F. (2008). Tectonic patterns on reoriented and despun planetary bodies. *Icarus*, *195*(1), 459–473. https://doi.org/10.1016/j.icarus.2007.12.003

McKinnon, W. B. (2006). On convection in ice I shells of outer solar system bodies, with specific application to Callisto. *Icarus*, *183*(2), 435–450. https://doi.org/10.1016/j.icarus.2006.03.004

McKinnon, W. B., & Parmentier, E. M. (1986). Ganymede and Callisto. In J. A. Burns & M. S. Mathews (Eds.), *Satellites* (pp. 718–763). Tucson, AZ: University of Arizona Press.

McNamara, A. K., & Zhong, S. (2005). Degree-one mantle convection: Dependence on internal heating and temperature-dependent rheology. *Geophysical Research Letters*, *32*, L01301. https://doi.org/10.1029/2004GL021082

McNutt, M. K. (1984). Lithospheric flexure and thermal anomalies. *Journal of Geophysical Research*, *89*(B13), 11,180–11,194. https://doi.org/10.1029/JB089iB13p11180

Moore, J. M., Chapman, C. R., Bierhaus, E. B., Greeley, R., Chuang, F. C., Klemaszewski, J., et al. (2004). Callisto. In F. Bagenal, T. E. Dowling, & W. B. McKinnon (Eds.), *Jupiter—The planet, satellites, and magnetosphere* (pp. 397–426). Cambridge, UK: Cambridge University Press.

Moore, J. M., Horner, V. M., & Greeley, R. (1985). The geomorphology of Rhea: Implications for geologic history and surface processes. *Journal of Geophysical Research*, *90*(S02), C785–C796. https://doi.org/10.1029/JB090iS02p0C785

Moore, W. B. (2008). Heat transport in a convecting layer heated fromwithin and below. *Journal of Geophysical Research*, *113*, B11407. https://doi.org/10.1029/2006JB004778

Moore, J. M., & Schenk, P. M. (2007). Topography of endogenic features on Saturnian mid-sized satellites, Lunar Planet. Sci. XXXVIII, #2136.

Moore, W. B. (2006). Thermal equilibrium in Europa's ice shell. *Icarus*, *180*, 141–146.

Moresi, L., & Solomatov, V. (1998). Mantle convection with a brittle lithosphere: Thoughts on the global tectonic style of the Earth and Venus. *Geophysical Journal International*, *133*(3), 669–682. https://doi.org/10.1046/j.1365-246X.1998.00521.x

Murray, C. D., & Dermott, S. F. (1999). *Solar System Dynamics*. New York: Cambridge University Press.

Nadeau, A., & McGehee, R. (2017). A simple formula for a planet's mean annual insolation by latitude. *Icarus*, *291*, 46–50. https://doi.org/10.1016/j.icarus.2017.01.040

Nimmo, F., & Manga, M. (2009). Geodynamics of Europa's ice shell. In R. T. Pappalardo, W. B. McKinnon, & K. Khurana (Eds.), *Europa after Galileo* (pp. 381–404). Tucson, AZ: University of Arizona Press.

Nimmo, F., & Pappalardo, R. T. (2006). Diapir-induced reorientation of Saturn's moon Enceladus. *Nature*, *441*(7093), 614–616. https://doi.org/10.1038/nature04821

Nimmo, F., Spencer, J. R., Pappalardo, R. T., & Mullen, M. E. (2007). Shear heating as the origin of the plumes and heat flux on Enceladus. *Nature*, *447*, 289–291. https://doi.org/10.1038/nature05783

O'Farrell, K. A., & Lowman, J. P. (2010). Emulating the thermal structure of spherical shell convection in plane-layer geometry mantle convection models. *Physics of the Earth and Planetary Interiors*, *182*(1-2), 73–84. https://doi.org/10.1016/j.pepi.2010.06.010

Ojakangas, G. W., & Stevenson, D. J. (1989). Thermal state of an ice shell on Europa. *Icarus*, *81*(2), 220–241. https://doi.org/10.1016/0019-1035(89)90052-3

O'Neill, C., & Nimmo, F. (2010). The role of episodic overturn in generating the surface geology and heat flow on Enceladus. *Nature Geoscience*, *3*(2), 88–91. https://doi.org/10.1038/NGEO731

Panning, M. P., Stähler, S. C., Huang, H.-H., Vance, S., Kedar, S., Tsai, V. C., & Pike, W. T. (2018). Expected seismicity and the seismic noise environment of Europa. *Journal of Geophysical Research: Planets*, *123*, 163–179. https://doi.org/10.1002/2017JE005332

Pappalardo, R. T., Collins, G. C., Head, J. W. III, Helfenstein, P., McCord, T., Moore, J. M., et al. (2004). Geology of Ganymede. In *Jupiter: The planet, satellites & magnetosphere* (pp. 363–396). New York: Cambridge University Press.

Pappalardo, R. T., Head, J. W., Greeley, R., Sullivan, R. J., Pilcher, C., Schubert, G., et al. (1998). Geological evidence for solid-state convection in Europa's ice shell. *Nature*, *391*(6665), 365–368. https://doi.org/10.1038/34862

Porco, C. C., Helfenstein, P., Thomas, P. C., Ingersoll, A. P., Wisdom, J., West, R., et al. (2006). Cassini observes the active south pole of Enceladus. *Science*, *311*(5766), 1393–1401. https://doi.org/10.1126/science.1123013

Quick, L. C., & Marsh, B. D. (2015). Constraining the thickness of Europa's water-ice shell: Insights from tidal dissipation and conductive cooling. *Icarus*, *253*, 16–24. https://doi.org/10.1016/j.icarus.2015.02.016

Roberts, J. H., & Nimmo, F. (2008). Near-surface heating on Enceladus and the south polar thermal anomaly. *Geophysical Research Letters*, *35*, L09201. https://doi.org/10.1029/2008GL033725

Rozel, A., Besserer, J., Golabek, G. J., Kaplan, M., & Tackley, P. J. (2014). Self-consistent generation of single-plume state for Enceladus using non-Newtonian rheology. *Journal of Geophysical Research: Planets*, *119*, 416–439. https://doi.org/10.1002/2013JE004473

Rudolph, M. L., & Manga, M. (2012). Effects of anisotropic viscosity and texture development on convection in ice mantles. *Journal of Geophysical Research*, *117*, E11003. https://doi.org/10.1029/2012JE004166

Sagan, C., & Mullen, G. (1972). Earth and Mars: Evolution of atmospheres and surface temperatures. *Science*, *177*(4043), 52–56. https://doi.org/10.1126/science.177.4043.52

Schenk, P., Hamilton, D. P., Johnson, R. E., McKinnon, W. B., Paranicas, C., Schmidt, J., & Showalter, M. R. (2011). Plasma, plumes and rings: Saturn system dynamics as recorded in global color patterns on its midsize icy satellites. *Icarus*, *211*(1), 740–757. https://doi.org/10.1016/j.icarus.2010.08.016

Schenk, P. M. (2017). True polar wander of Enceladus from topographic data. *Icarus*, *295*, 46–60. https://doi.org/10.1016/j.icarus.2017.04.019

Schenk, P. M., & McKinnon, W. B. (2009). One-hundred-km-scale basins on Enceladus: Evidence for an active ice shell. *Geophysical Research Letters*, *36*, L16202. https://doi.org/10.1029/2009GL039916

Schubert, G., & Anderson, C. A. (1985). Finite element calculations of very high Rayleigh number thermal convection. *Geophysical Journal of the Royal Astronomical Society*, *80*(3), 575–601. https://doi.org/10.1111/j.1365-246X.1985.tb05112.x

Schubert, G., Anderson, J. D., Travis, B. J., & Palguta, J. (2007). Enceladus: Present internal structure and differentiation by early and long-term radiogenic heating. *Icarus*, *188*(2), 345–355. https://doi.org/10.1016/j.icarus.2006.12.012

Schubert, G., Turcotte, D. L., & Olson, P. (2001). *Mantle Convection in the Earth and Planets*. New York: Cambridge University Press.

Schmidt, B. E., Blankenship, D. D., Patterson, G. W., & Schenk, P. M. (2011). Active formation of 'chaos terrain' over shallow subsurfacewater on Europa. *Nature*, *479*, 502–505. https://doi.org/10.1038/nature10608

Showman, A. P., & Han, L. (2004). Numerical simulations of convection in Europa's ice shell: Implications for surface features. *Journal of Geophysical Research*, *109*, E01010. https://doi.org/10.1029/2003JE002103

Showman, A. P., & Han, L. (2005). Effects of plasticity on convection in an ice shell: Implications for Europa. *Icarus*, *177*(2), 425–437. https://doi.org/10.1016/j.icarus.2005.02.020

Showman, A. P., Han, L., & Hubbard, W. B. (2013). The effect of an asymmetric core on convection in Enceladus' ice shell: Implications for south polar tectonics and heat flux. *Geophysical Research Letters*, *40*, 5610–5614. https://doi.org/10.1002/2013GL057149

Smith, B. A., Soderblom, L. A., Beebe, R., Bliss, D., Brown, R. H., Collins, S. A., et al. (1986). Voyager 2 in the Uranian system: Imaging science results. *Science*, *233*, 43–64.

Sotin, C., Head, J. W. III, & Tobie, G. (2002). Europa: Tidal heating of upwelling thermal plumes and the origin of lenticulae and chaos melting. *Geophysical Research Letters*, *29*(8), 1233. https://doi.org/10.1029/2001GL013844

Sotin, C., Tobie, G., Wahr, J., & McKinnon, W. B. (2009). Tides and tidal heating on Europa. In R. T. Pappalardo, W. B. McKinnon, & K. Khurana (Eds.), *Europa* (pp. 85–118). Tucson, AZ: University of Arizona Press.

Sparks, W. B., Schmidt, B. E., McGrath, M. A., Hand, K. P., Spencer, J. R., Cracraft, M., & Deustua, S. E. (2017). Active cryovolcanism on Europa? *Astrophysical Journal Letters*, *839*(2), L18. https://doi.org/10.3847/2041-8213/aa67f8

Spencer, J. R., Barr, A. C., Esposito, L. W., Helfenstein, P., Ingersoll, A. P., Jaumann, R., et al. (2009). Enceladus: An active cryovolcanic satellite. In M. K. Dougherty, L. W. Esposito, & S. M. Krimigis (Eds.), *Saturn after Cassini-Huygens* (pp. 683–724). New York: Springer.

Spitale, J. N., & Porco, C. C. (2007). Association of the jets of Enceladus with the warmest regions on its south polar fractures. *Nature*, *449*(7163), 695–697. https://doi.org/10.1038/nature06217

Squyres, S. W. (1980). Surface temperatures and retention of H_2O frost on Ganymede and Callisto. *Icarus*, *44*(2), 502–510. https://doi.org/10.1016/0019-1035(80)90040-8

Tajeddine, R., Soderlund, K. M., Thomas, P. C., Helfenstein, P., Hedman, M. M., Burns, J. A., & Schenk, P. M. (2017). True polar wander of Enceladus from topographic data. *Icarus*, *295*, 46–60. https://doi.org/10.1016/j.icarus.2017.04.019

Tobie, G., Grasset, O., Lunine, J. I., Mocquet, A., & Sotin, C. (2005). Titan's internal structure inferred from a coupled thermal-orbital model. *Icarus*, *175*(2), 496–502. https://doi.org/10.1016/j.icarus.2004.12.007

Tosi, N., Cadek, O., Behounková, M., Kánová, M., Plesa, A.-C., Grott, M., et al. (2015). Mercury's low-degree geoid and topography controlled by insolation-driven elastic deformation. *Geophysical Research Letters*, *42*, 7327–7335. https://doi.org/10.1002/2015GL065314

Turcotte, D. L., & Schubert, G. (2005). *Geodynamics* (2nd ed.). New York: Cambridge University Press.

Vance, S. D., Kedar, S., Panning, M. P., Stahler, S. C., Bills, B. G., Lorenz, R. D., et al. (2018). Vital signs: Seismology of icy ocean worlds. *Astrobiology*, *18*(1), 37–53. https://doi.org/10.1089/ast.2016.1612

van Summeren, J., Conrad, C. P., & Gaidos, E. (2011). Mantle convection, plate tectonics, and volcanism on hot exo-Earths. *Astrophysical Journal Letters*, *736*(1), L15. https://doi.org/10.1088/2041-8205/736/1/L15

Wagner, R., Neukum, G., Giese, B., Roatsch, T., Wolf, U., & Denk, T. (2006). Geology, ages and topography of Saturn's satellite Dione observed by the Cassini ISS camera, Lunar Planet. Sci. XXXVII, #1805.

Wahr, J., Selvans, Z. A., Mullen, M. E., Barr, A. C., Collins, G. C., & Selvans, M. M. (2009). Modeling stresses on satellites due to nonsynchronous rotation and orbital eccentricity using gravity potential theory. *Icarus*, *200*(1), 188–206. https://doi.org/10.1016/j.icarus.2008.11.002

Walker, C. C., Bassis, J. N., & Liemohn, M. W. (2012). On the application of simple rift basin models to the south polar region of Enceladus. *Journal of Geophysical Research*, *117*, E07003. https://doi.org/10.1029/2012JE004084

Weller, M. B., Fuchs, L., Becker, T. W., & Soderlund, K. M. (2019). Convection in thin shells of icy satellites: Effects of latitudinal surface temperature variations; figure data, [data set]. *Zenodo*. https://doi.org/10.5281/zenodo.2580256

Weller, M. B., & Lenardic, A. (2016). The energetics and convective vigor of mixed-mode heating: Scaling and implications for the tectonics of exoplanets. *Geophysical Research Letters*, *43*, 9469–9474. https://doi.org/10.1002/2016GL069927

Weller, M. B., Lenardic, A., & Moore, W. B. (2016). Scaling relationships and physics for mixed heating convection in planetary interiors: Isoviscous spherical shells. *Journal of Geophysical Research: Solid Earth*, *121*, 7598–7617. https://doi.org/10.1002/2016JB013247

Whitaker, E. A., & Greenberg, R. J. (1973). Eccentricity and inclination of Miranda's orbit. *Monthly Notices of the Royal Astronomical Society*, *165*(1), 15P–18P. https://doi.org/10.1093/mnras/165.1.15P

Yao, C., Deschamps, F., Lowman, J. P., Sanchez-Valle, C., & Tackley, P. J. (2014). Stagnant lid convection in bottom-heated thin 3-D spherical shells: Influence of curvature and implications for dwarf planets and icy moons. *Journal of Geophysical Research: Planets*, *119*, 1895–1913. https://doi.org/10.1002/2014JE004653

Zahnle, K., Schenk, P., Levison, H., & Dones, L. (2003). Cratering rates in the outer solar system. *Icarus*, *163*(2), 263–289. https://doi.org/10.1016/S0019-1035(03)00048-4

Zhong, S., McNamara, A. K., Tan, E., Moresi, L., & Gurnis, M. (2008). A benchmark study on mantle convection in a 3-D spherical shell using CitcomS. *Geochemistry, Geophysics, Geosystems*, *9*, Q10017. https://doi.org/10.1029/2008GC002048

Zhong, S., Zuber, M. T., Moresi, L., & Gurnis, M. (2000). Role of temperature dependent viscosity and surface plates in spherical shell models of mantle convection. *Journal of Geophysical Research*, *105*, 11,063–11,082. https://doi.org/10.1029/2000JB900003

References From the Supporting Information

Baland, R.-M., Yseboodt, M., & Van Hoolst, T. (2016). The obliquity of Enceladus. *Icarus*, *268*, 12–31. https://doi.org/10.1016/j.icarus.2015.11.039